

# Description of the NASA GEOS Composition Forecast Modeling System GEOS-CF v1.0

Christoph A. Keller<sup>1</sup>, K. Emma Knowland<sup>1</sup>, Bryan N Duncan<sup>2</sup>, Junhua Liu<sup>1</sup>, Daniel C Anderson<sup>1</sup>, Sampa Das<sup>2</sup>, Robert A Lucchesi<sup>3</sup>, Elizabeth W Lundgren<sup>4</sup>, Julie M. Nicely<sup>2</sup>, Jon Eric Nielsen<sup>5</sup>, Lesley E. Ott<sup>2</sup>, Emily Saunders<sup>3</sup>, Sarah A. Strode<sup>6</sup>, Pamela A Wales<sup>7</sup>, Daniel J. Jacob<sup>4</sup>, and Steven Pawson<sup>2</sup>

<sup>1</sup>Universities Space Research Association

<sup>2</sup>NASA Goddard Space Flight Center

<sup>3</sup>Science Systems and Applications, Inc

<sup>4</sup>Harvard University

<sup>5</sup>SSAI at NASA Goddard Space Flight Center

<sup>6</sup>Universities Space Research Association

<sup>7</sup>University of Maryland, College Park

November 22, 2022

## Abstract

The Goddard Earth Observing System composition forecast (GEOS-CF) system is a high-resolution (0.25 degree) global constituent prediction system from NASA's Global Modeling and Assimilation Office (GMAO). GEOS-CF offers a new tool for atmospheric chemistry research, with the goal to supplement NASA's broad range of space-based and in-situ observations and to support flight campaign planning, support of satellite observations, and air quality research. GEOS-CF expands on the GEOS weather and aerosol modeling system by introducing the GEOS-Chem chemistry module to provide analyses and 5-day forecasts of atmospheric constituents including ozone (O<sub>3</sub>), carbon monoxide (CO), nitrogen dioxide (NO<sub>2</sub>), and fine particulate matter (PM<sub>2.5</sub>). The chemistry module integrated in GEOS-CF is identical to the offline GEOS-Chem model and readily benefits from the innovations provided by the GEOS-Chem community.

Evaluation of GEOS-CF against satellite, ozonesonde and surface observations show realistic simulated concentrations of O<sub>3</sub>, NO<sub>2</sub>, and CO, with normalized mean biases of -0.1 to -0.3, normalized root mean square errors (NRMSE) between 0.1-0.4, and correlations between 0.3-0.8. Comparisons against surface observations highlight the successful representation of air pollutants under a variety of meteorological conditions, yet also highlight current limitations, such as an overprediction of summertime ozone over the Southeast United States. GEOS-CF v1.0 generally overestimates aerosols by 20-50% due to known issues in GEOS-Chem v12.0.1 that have been addressed in later versions.

The 5-day hourly forecasts have skill scores comparable to the analysis. Model skills can be improved significantly by applying a bias-correction to the surface model output using a machine-learning approach.

1 **Description of the NASA GEOS Composition Forecast Modeling System GEOS-CF**  
2 **v1.0**

3 **Christoph A. Keller<sup>1</sup>, K. Emma Knowland<sup>1,2</sup>, Bryan N. Duncan<sup>1</sup>, Junhua Liu<sup>1,2</sup>, Daniel C.**  
4 **Anderson<sup>1,2</sup>, Sampa Das<sup>1,2</sup>, Robert A. Lucchesi<sup>1,3</sup>, Elizabeth W. Lundgren<sup>4</sup>, Julie M.**  
5 **Nicely<sup>1,5</sup>, Eric Nielsen<sup>1,3</sup>, Lesley E. Ott<sup>1</sup>, Emily Saunders<sup>1,3</sup>, Sarah A. Strode<sup>1,2</sup>, Pamela A.**  
6 **Wales<sup>1,2</sup>, Daniel J. Jacob<sup>4</sup>, Steven Pawson<sup>1</sup>**

7 <sup>1</sup>NASA Goddard Space Flight Center, Greenbelt, MD, USA

8 <sup>2</sup>Universities Space Research Association, Columbia, MD, USA

9 <sup>3</sup>Science Systems and Applications, Inc., Lanham, MD, USA

10 <sup>4</sup>School of Engineering and Applied Sciences, Harvard University, Cambridge, MA, USA

11 <sup>5</sup>Science Systems and Applications, Inc., Lanham, MD, USA

12  
13 Corresponding author: Christoph Keller ([christoph.a.keller@nasa.gov](mailto:christoph.a.keller@nasa.gov))

14 **Key Points:**

- 15 • GEOS-CF is a new modeling system that produces global forecasts of atmospheric  
16 composition at 25km<sup>2</sup> horizontal resolution.
- 17 • GEOS-CF model output is freely available and offers a new tool for academic  
18 researchers, air quality managers, and the public.
- 19

## 20 **Abstract**

21 The Goddard Earth Observing System composition forecast (GEOS-CF) system is a high-  
22 resolution (0.25 degree) global constituent prediction system from NASA's Global Modeling and  
23 Assimilation Office (GMAO). GEOS-CF offers a new tool for atmospheric chemistry research,  
24 with the goal to supplement NASA's broad range of space-based and in-situ observations and to  
25 support flight campaign planning, support of satellite observations, and air quality research.  
26 GEOS-CF expands on the GEOS weather and aerosol modeling system by introducing the  
27 GEOS-Chem chemistry module to provide analyses and 5-day forecasts of atmospheric  
28 constituents including ozone (O<sub>3</sub>), carbon monoxide (CO), nitrogen dioxide (NO<sub>2</sub>), and fine  
29 particulate matter (PM<sub>2.5</sub>). The chemistry module integrated in GEOS-CF is identical to the  
30 offline GEOS-Chem model and readily benefits from the innovations provided by the GEOS-  
31 Chem community.

32 Evaluation of GEOS-CF against satellite, ozonesonde and surface observations show realistic  
33 simulated concentrations of O<sub>3</sub>, NO<sub>2</sub>, and CO, with normalized mean biases of -0.1 to -0.3,  
34 normalized root mean square errors (NRMSE) between 0.1-0.4, and correlations between 0.3-  
35 0.8. Comparisons against surface observations highlight the successful representation of air  
36 pollutants under a variety of meteorological conditions, yet also highlight current limitations,  
37 such as an overprediction of summertime ozone over the Southeast United States. GEOS-CF  
38 v1.0 generally overestimates aerosols by 20-50% due to known issues in GEOS-Chem v12.0.1  
39 that have been addressed in later versions.

40 The 5-day hourly forecasts have skill scores comparable to the analysis. Model skills can be  
41 improved significantly by applying a bias-correction to the surface model output using a  
42 machine-learning approach.

## 43 **Plain Language Summary**

44 Accurate forecasting of the composition of the atmosphere is important for a variety of  
45 applications, including air pollution mitigation, support of satellite and other remote-sensing  
46 observations, and research applications. Producing such forecasts is computationally expensive  
47 due to the complexity of atmospheric chemistry, which interacts with weather on all scales. Here  
48 we present the NASA Goddard Earth Observing System composition forecast (GEOS-CF)  
49 system, which produces global forecasts of major atmospheric constituents such as ozone (O<sub>3</sub>),  
50 nitrogen dioxide (NO<sub>2</sub>), and fine particulate matter (PM<sub>2.5</sub>). On a daily basis, the model tracks  
51 the atmospheric concentrations of more than 250 chemical species in more than 55 million model  
52 grid cells, computing the interactions between those species using the state-of-the-science  
53 GEOS-Chem chemistry model.

54 We present an in-depth evaluation of the GEOS-CF model through comparison against  
55 independent observations. We show how the model captures many observed features of  
56 atmospheric composition, such as spatio-temporal variations in air pollution due to changes in  
57 pollutant emissions, weather, and chemistry. We also highlight some of the model deficiencies,  
58 e.g., with respect to the simulation of aerosol particles. Finally, we demonstrate how surface  
59 observations and model data can be combined using machine learning to provide improved local  
60 air quality forecasts.

## 61 **1 Introduction**

62 Near real-time information of global atmospheric composition is invaluable for a wide  
63 range of applications, including academic research, airborne and satellite mission support, air

64 quality forecasting, disaster management, and ecosystem monitoring. However, the numerical  
65 simulation of atmospheric chemistry is computationally expensive because it involves hundreds  
66 of species that interact with each other on time scales from milliseconds to years, and the species  
67 are also influenced by dynamics across a wide range of spatiotemporal scales. This precludes the  
68 inclusion of detailed aerosol and reactive trace gases in standard operational numerical weather  
69 prediction (NWP) systems. Instead, real-time simulation of atmospheric composition is typically  
70 done within a simplified system in order to reduce the computational burden, e.g., by running the  
71 model at reduced horizontal resolution or over a regional domain only, using a simplified  
72 representation of atmospheric composition, or by coupling a weather model with an offline  
73 chemical transport model (CTM) (e.g., Bhattacharjee et al., 2018; Emmons et al., 2020;  
74 Flemming et al., 2015; Marécal et al., 2015).

75  
76 Here we present the NASA Goddard Earth Observing System (GEOS) composition  
77 forecast modeling system, GEOS-CF v1.0, which provides global analyses and forecasts of  
78 atmospheric composition such as ozone (O<sub>3</sub>), carbon monoxide (CO), nitrogen dioxide (NO<sub>2</sub>),  
79 and fine particulate matter (PM<sub>2.5</sub>) in near real-time at a horizontal resolution of approximately  
80 25x25 km<sup>2</sup>. To our knowledge, GEOS-CF is one of only a few global forecasting systems of  
81 atmospheric composition conducted in near real-time. The European Centre for Medium-Range  
82 Weather Forecasts (ECMWF) offers 5-day global forecasts of aerosols and trace gases at  
83 approximately 40x40 km<sup>2</sup> horizontal resolution through the Copernicus Atmosphere Monitoring  
84 Service (CAMS, <https://atmosphere.copernicus.eu/global-forecast-plots>). The US National  
85 Center for Atmospheric Research (NCAR) conducts 10-day global forecasts at approximately  
86 100x100 km<sup>2</sup> horizontal resolution based on offline simulations of the Model for Ozone and  
87 Related chemical Tracers (MOZART) Chemistry Mechanism in the Community Earth System  
88 Model Version 2 (CESM2) (Emmons et al., 2020) driven by GEOS meteorological forecasts  
89 (<https://www2.acom.ucar.edu/acresp/forecasts-and-near-real-time-nrt-products>). Finally, the  
90 Finnish Meteorological Institute provides daily 4-day global forecasts of atmospheric  
91 composition at approximately 35x35 km<sup>2</sup> resolution using the System for Integrated modeLling  
92 of Atmospheric coMposition (SILAM v5.7, <http://silam.fmi.fi/>). The atmospheric composition  
93 forecasts from these models can vary considerably due to differences in the underlying  
94 meteorological fields, observational constraints, chemical mechanisms, or assumptions about  
95 pollutant emissions. The uncertainties associated with these processes can be difficult to quantify  
96 from a single model simulation alone, and the availability of multiple, independently developed  
97 models offers great potential to provide better air quality information through combination of a  
98 suite of models (Marécal et al., 2015). GEOS-CF offers such an independent composition  
99 forecast, thus complementing the existing suite of global composition forecasting systems by  
100 providing global 5-day forecasts of atmospheric composition using the GEOS-Chem atmospheric  
101 chemistry module (<http://www.geos-chem.org>) within GEOS from January 2018 onward.

102  
103 One of the key aspects of the GEOS-CF system is the full integration of the GEOS-Chem  
104 model in the GEOS system, which allows for the simulation of reactive gases and aerosols at the  
105 same temporal and spatial resolution as the meteorology (Long et al., 2015; Hu et al., 2018).  
106 GEOS-Chem is actively evaluated and developed by a large international research community,  
107 and the GEOS-Chem module incorporated in GEOS-CF uses the exact same codebase as the  
108 offline CTM. This enables the seamless integration of scientific updates provided by the GEOS-  
109 Chem CTM community into GEOS-CF without the need to make any modifications to the source

110 code. The scientific validity of the GEOS-Chem chemistry module within GEOS has been  
111 demonstrated by Hu et al. (2018), who show that a one-year global simulation of atmospheric  
112 composition at 12.5 km<sup>2</sup> produces results consistent with the offline GEOS-Chem model. GEOS-  
113 CF is a natural extension of the online GEOS-Chem module embedded in GEOS, with a focus on  
114 daily operation and forecast capabilities.

115  
116 GEOS-CF is the latest in a series of research and applications products generated by the  
117 NASA Global Modeling and Assimilation Office (GMAO), including the GEOS forward  
118 processing weather and aerosol system (GEOS FP), GEOS FP for instrument teams (GEOS FP-  
119 IT, Lucchesi, 2015), the second Modern-Era Retrospective analysis for Research and  
120 Applications (MERRA-2, Gelaro et al., 2017), and the Seasonal to Subseasonal Forecasting  
121 System (GEOS-S2S, Borovikov et al., 2019; Molod et al., 2020). It leverages GMAO's model  
122 infrastructure and directly builds on a number of development activities centered around the  
123 GEOS model, with the goal to extend these forecasting capabilities toward (short-lived) trace  
124 gases and aerosols.

125 GEOS is a General Circulation Model (GCM) and Data Assimilation System (DAS) consisting  
126 of a suite of model components that can be connected in a modular manner through the Earth  
127 System Modeling Framework (ESMF, Hill et al., 2004) and Modeling Analysis and Prediction  
128 Layer (MAPL, Suarez et al., 2007) software interface. The model can be configured to run with  
129 fully interactive chemistry so that the chemical constituents feed back to the dynamics ('online'),  
130 or as an offline model where external meteorological fields are used as input. A hybrid approach  
131 is the 'replay' feature, where the model dynamics are nudged toward pre-computed analysis  
132 fields (from a previous DAS simulation) in a way that is consistent with the internal physics of  
133 the model (Orbe et al., 2017). This approach is particularly useful for chemistry simulations as it  
134 sidesteps the need to conduct a computationally costly meteorological data assimilation cycle.  
135 Several chemistry and aerosol modules of varying complexity are available in GEOS (Nielsen et  
136 al., 2017), enabling a wide range of applications including: near real-time simulation of aerosols  
137 using the GOCART module (Colarco et al. 2010; Randles et al., 2017; Buchard et al., 2017),  
138 computationally efficient analysis of stratospheric ozone using parameterized chemistry in  
139 combination with 3D-Variational assimilation of satellite observations (Wargan et al., 2015);  
140 multi-decade simulation of tropospheric and stratospheric chemistry using the Global Modeling  
141 Initiative (GMI) chemistry module (Douglass et al., 2004; Duncan et al., 2007, Strahan et al.,  
142 2007); and fully coupled simulation of gas-phase and aerosol chemistry using the GEOS-Chem  
143 chemistry module embedded in GEOS (Long et al., 2015).

144  
145 In this paper we describe the configuration of GEOS-CF version 1.0 (Section 2) and  
146 demonstrate the validity of the produced analyses through comparison against independent  
147 observations (Sections 3-4). Model forecasts are evaluated in Section 5 and we discuss how  
148 model skill scores can be improved by applying a bias-correction to the surface observations  
149 using a machine-learning approach. As described in detail below, the current version of GEOS-  
150 CF constitutes a hybrid model between an online weather and chemistry assimilation system and  
151 an offline CTM application, with a development pathway toward a fully coupled forecasting  
152 system with integrated trace gases and aerosols. Many of its design features were guided by  
153 practical considerations as well as computational limitations related to the simulation of  
154 atmospheric chemistry.

## 155 2 Model Description

### 156 2.1. General Description

157 A schematic of the GEOS-CF v1.0 modeling system is provided in Figure 1. GEOS-CF is  
158 operated in near real-time, producing a 5-day forecast once a day. The forecast initial conditions  
159 are provided by a one-day replay simulation (i.e., ‘analysis’) constrained by pre-computed  
160 meteorological analysis fields. In the v1.0 configuration, the analysis forcings that GEOS-CF  
161 uses are GEOS FP-IT meteorological variables and GOCART aerosols providing meteorological  
162 feedbacks, and GEOS-FP stratospheric ozone (described below). All other trace gases are  
163 integrated without observational constraints. The resulting model conditions at the end of the  
164 simulated day also serve as input for the next day's replay step (i.e., restart files). This preserves  
165 the model chemical and meteorological state from one forecast cycle to the next, leading to a  
166 continuous atmospheric composition archive since January 2018.

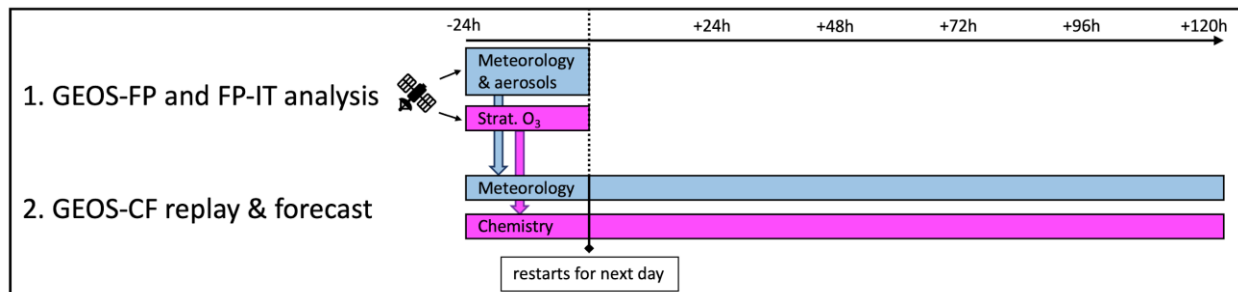
167 GEOS FP-IT is a ‘frozen’ model system that is comparable to MERRA-2 but - unlike  
168 MERRA-2 - is available in near real-time to support retrievals by satellite instrument teams. The  
169 GEOS model in general, and version of the GEOS GCM used by GEOS FP-IT (v5.12.4) in  
170 particular, has shown to be well suited for atmospheric chemistry applications as it realistically  
171 captures features critical to atmospheric composition, such as the seasonal climate of moisture  
172 and temperature and large-scale transport of constituents (e.g., Pawson et al., 2007; Douglass et  
173 al., 2014; Oman and Douglass, 2014; Molod et al., 2015; Gelaro et al., 2017).

174  
175 GEOS-CF v1.0 uses a model physics package that is similar to MERRA-2 and GEOS FP-  
176 IT, consisting of the GEOS atmospheric model, version 5, described in Rienecker et al. (2008)  
177 with updates as described in Molod et al. (2012) and Molod et al. (2015). The model uses the  
178 finite-volume dynamical core of Lin (2004) with a cubed sphere grid discretization to avoid grid-  
179 cell singularities (Putman and Lin, 2007). It is run at cubed-sphere c360 horizontal resolution  
180 (roughly equivalent to  $0.25^\circ \times 0.25^\circ$ ) and 72 hybrid-eta levels from the surface to 0.01 hPa.  
181 Model physics includes parameterizations for moist processes, radiation, turbulent mixing, land-  
182 surface processes, and gravity wave drag. The moist module contains parameterization of  
183 convection using the Relaxed Arakawa-Schubert scheme (Moorthi & Suarez, 1992), and the  
184 single-moment parameterization for large-scale precipitation and cloud cover described in  
185 Bacmeister et al. (2006). The radiation module includes parameterization for long-wave (Chou  
186 1990, 1992) and short-wave radiation processes (Chou and Suarez 1994). Turbulence is  
187 parameterized using the gradient Richardson number in the free atmosphere and the Lock  
188 scheme (Lock et al., 2000) interfaced with the scheme of Louis and Geleyn (1982) in the  
189 boundary layer. Exchange of heat, moisture and momentum between land, atmosphere, and  
190 ocean or sea ice surfaces are parameterized using Monin-Obukhov similarity theory (Helfand  
191 and Schubert, 1995, Molod et al., 2013), and the gravity wave drag parameterization contains  
192 orographic (McFarlane, 1987) and non-orographic (Garcia & Boville, 1994) waves.

193  
194 In the GEOS-CF system, the GEOS physics components are coupled to the GOCART  
195 aerosol component to provide consistent physics with the GEOS FP-IT meteorology. The GEOS-  
196 Chem chemistry module is run “passively” to provide coupled aerosol-oxidant chemistry in the  
197 troposphere and stratosphere (Hu et al., 2018). The GOCART aerosols, constrained during the  
198 replay step by aerosol optical depth (AOD) observations from the Moderate Resolution Imaging  
199 Spectroradiometer (MODIS) aboard the Terra and Aqua satellites (Randles et al., 2017), are used

200 to compute the feedback between aerosols and dynamics. This ensures consistency between  
 201 GEOS-CF and the GEOS FP-IT analysis fields. Currently, there is no chemical coupling between  
 202 GOCART and GEOS-Chem, and no observations are directly assimilated into GEOS-CF.  
 203 However, stratospheric ozone in GEOS-Chem is nudged towards ozone produced by GEOS FP,  
 204 which is constrained by ozone measurements from the Microwave Limb Sounder (MLS), Ozone  
 205 Monitoring Instrument (OMI), and NASA's Ozone Mapping and Profiler Suite (OMPS) and  
 206 produces a realistic analysis of ozone in the stratosphere (Wargan et al., 2015; 2020). In addition,  
 207 near real-time MODIS observations of fire radiative power are used to constrain fire emissions,  
 208 as produced by the Quick Fire Emissions Dataset (QFED) (Darmenov and Da Silva, 2015).

209 All computations are conducted on the Discover supercomputing cluster of the NASA  
 210 Center for Climate Simulation (NCCS). Run on 3510 Intel Xeon Haswell processor cores, the  
 211 one-day analysis and 5-day forecast takes approximately 8.5 wall-clock hours. GEOS-CF  
 212 analysis and forecast output includes chemistry and meteorology "surface" output every 15  
 213 minutes as well as hourly-average and instantaneous fields for surface, column-average, and 3-  
 214 dimensional model output. The model output is publicly available at  
 215 [https://gmao.gsfc.nasa.gov/weather\\_prediction/GEOS-CF/data\\_access/](https://gmao.gsfc.nasa.gov/weather_prediction/GEOS-CF/data_access/) in the form of on-demand  
 216 figures or through access to the model output (in netCDF data format) via Hypertext Transfer  
 217 Protocol (HTTP) file download or through the Open-source Project for a Network Data Access  
 218 Protocol (OPeNDAP) remote access tool. The full 5-day model forecast output is publicly  
 219 available for a duration of 14 days. Given the growing interest in air quality forecasting  
 220 applications, the model forecasts for a selection of surface air pollutants are made available on  
 221 the public portal indefinitely. Full details on available output and data access are available in the  
 222 GEOS-CF File Specification document (Knowland et al., 2020).  
 223



224 **Figure 1.** Schematic of the GEOS-CF modeling system approach, consisting of one day analysis  
 225 and 5-day forecast. This combination of simulations is conducted on a daily basis.  
 226

## 227 2.2. Chemistry

228 GEOS-CF v1.0 uses the continually updated standard version of the GEOS-Chem  
 229 chemistry module to simulate coupled aerosol-oxidant chemistry in the troposphere and  
 230 stratosphere. The current version 12.9.2 of GEOS-Chem has been implemented into GEOS-CF  
 231 as of this writing, but results are presented here for version 12.0.1 in order to have a two-year  
 232 record for comparison to observations. GEOS-Chem is ESMF-compliant and its chemistry  
 233 module is implemented here as an ESMF gridded component of GEOS, as described in Long et  
 234 al. (2015) and Hu et al. (2018).

235 The gas-phase chemistry scheme includes detailed tropospheric chemistry of HO<sub>x</sub>, NO<sub>x</sub>, BrO<sub>x</sub>,  
 236 volatile organic compounds (VOC), and O<sub>3</sub>, as originally described by Bey et al. (2001), with  
 237 addition of halogen chemistry by Parrella et al. (2012) and Sherwen et al. (2016) plus updates to

238 isoprene oxidation as described by Mao et al. (2013) and Miller et al. (2017). Stratospheric  
 239 chemistry is fully coupled with tropospheric chemistry through the Unified tropospheric-  
 240 stratospheric Chemistry eXtension (UCX, Eastham et al. (2014)) and extends to the top of the  
 241 atmosphere. Photolysis rates are computed by GEOS-Chem using the Fast-JX code (Bian and  
 242 Prather, 2002). The gas-phase mechanism comprises 250 chemical species and 725 reactions and  
 243 is solved using the Kinetic PreProcessor KPP Rosenbrock solver (Sandu and Sander, 2006). The  
 244 aerosol simulation includes sulfate-nitrate-ammonia chemistry (Park et al., 2004), black carbon  
 245 (Park et al., 2003; Wang et al., 2014), organic aerosols (Marais et al., 2016), mineral dust (Fairlie  
 246 et al., 2007; Ridley et al., 2012), and sea salt aerosols (Jaeglé et al., 2011). Aerosol and gas-phase  
 247 chemistry interact through gas-aerosol partitioning (Fountoukis and Nenes, 2007; Pye et al.,  
 248 2009), heterogeneous chemistry on aerosol surface (Evans and Jacob, 2005; Mao et al., 2013),  
 249 and aerosol impacts on photolysis (Martin et al., 2003). Methane concentrations are prescribed as  
 250 monthly mean surface concentrations, spatially interpolated from NOAA GLOBALVIEW flask  
 251 data (Dlugokencky et al., 1995).

### 252 2.3. Emissions and Deposition

253 The dry deposition scheme in GEOS-Chem is based on the resistance-in-series model of  
 254 Wesely (1989). Wet deposition of aerosols and soluble gases includes scavenging in convective  
 255 updrafts, in-cloud rainout, and below-cloud washout (Liu et al., 2001; Amos et al., 2012). All  
 256 emission calculations are done using the Harmonic Emissions Component HEMCO v2.1.009  
 257 (Keller et al., 2014). Table 1 summarizes the emission configuration used by GEOS-CF v1.0.  
 258 Anthropogenic emissions are broken down into hourly values using sector-specific day-of-week  
 259 and diurnal scale factors (van der Gon et al., 2011). In addition, an annual gridded scale factor  
 260 based on the Open-source Data Inventory for Anthropogenic CO<sub>2</sub> (ODIAC; Oda et al., 2017) is  
 261 applied to the anthropogenic emissions of CO.

262  
 263 **Table 1.** *Emissions used by GEOS-CF.*

Description	Reference	Comments
<i>Offline inventories</i>		
Anthropogenic NO, CO, black carbon (BC), organic carbon (OC), Ammonia (NH <sub>3</sub> )	HTAP v2.2 (Janssens-Maenhout et al., 2015)	Global except Africa
Anthropogenic SO <sub>2</sub>	OMI-HTAP (Liu et al., 2018)	Global except Africa
Anthropogenic VOCs	RETRO (Schultz et al., 2008)	Global except Africa
Anthropogenic NO, CO, SO <sub>2</sub> , BC, OC, NH <sub>3</sub> , VOCs	DICE-Africa (Marais and Wiedinmyer, 2016)	Africa
Arctic seabird NH <sub>3</sub>	Croft et al. (2016)	
Volcanic SO <sub>2</sub>	Carn (2019)	5% of the sulfur emitted as SO <sub>4</sub>
Aircraft NO <sub>x</sub> , CO, SO <sub>2</sub> , VOCs, BC, OC	AEIC (Stettler et al., 2011)	
<i>Dynamic emissions</i>		
Biogenic VOCs	MEGAN v2.1 (Guenther et al., 2012)	
Biomass burning NO <sub>x</sub> , CO, SO <sub>2</sub> , VOCs, BC, OC	QFED v2.5 (Darmenov and da Silva, 2015)	35% emitted between 3.5 and 5.5 km altitude (Fischer et al., 2014).
Lightning NO <sub>x</sub>	Murray et al., 2012	
Soil NO <sub>x</sub>	Hudman et al., 2012	
Soil dust	Zender et al., 2003	

Sea salt aerosols	Gong, 2003; Jaeglé et al., 2011	
Oceanic DMS, CH <sub>2</sub> O, C <sub>3</sub> H <sub>6</sub> O	Johnson, 2010; Nightingale et al., 2000	
Oceanic iodine	Carpenter et al., 2013	

### 264 3 Observations used for Model Evaluation

265 GEOS-CF is intended to supplement NASA's broad range of space-based and in-situ  
 266 observations, providing a new tool for researchers, government scientists, and air quality  
 267 managers. We therefore focus our evaluation on the species most pertinent to these applications,  
 268 including O<sub>3</sub>, NO<sub>2</sub>, CO, and aerosols. These species are also constantly evaluated by the broader  
 269 GEOS-Chem community using the standard CTM simulations (e.g., Hu et al., 2017, 2018; Travis  
 270 et al., 2019). However, it should be noted that GEOS-CF simulations can differ from standard  
 271 GEOS-Chem simulations due to the higher horizontal resolution and differences in the emission  
 272 inputs, in particular wildfire emissions (Hu et al., 2018).

273 We first evaluate the ability of the GEOS-CF analysis to provide a realistic representation  
 274 of atmospheric composition based on the hourly-average analysis fields (Section 4). Differences  
 275 between the 5-day model forecasts and the model analysis are discussed in Section 5.

276  
 277 The data sets used for model validation are summarized in Table 2. Briefly, we evaluate  
 278 the global tropospheric distribution of O<sub>3</sub> against ozonesonde observations obtained from the  
 279 World Ozone and Ultraviolet Data Center (WOUDC, <http://www.woudc.org>), NO<sub>2</sub> against the  
 280 OMI NASA standard tropospheric column NO<sub>2</sub> product v4.0 (Lamsal et al., 2020), CO total  
 281 columns against satellite retrievals from the Measurements Of Pollution In The Troposphere  
 282 (MOPITT) V8 (Deeter et al., 2019), and AOD against the Aerosol Robotic Network  
 283 (AERONET) level 2.0 daily average data from the version 3 data product  
 284 (<https://aeronet.gsfc.nasa.gov/>; Giles et al., 2019). In addition, we compare simulated surface  
 285 concentrations against in-situ observations from the Global Atmospheric Watch (GAW) World  
 286 Data Center for Greenhouse Gases (WDCGG, <https://gaw.kishou.go.jp/>) and World Data Centre  
 287 for Reactive Gases (WDCRG, <https://www.gaw-wdcr.org/>), as well as observations from the  
 288 OpenAQ database (<https://openaq.org>). For NO<sub>2</sub>, we omitted mountainous GAW sites given that  
 289 the model resolution of 25x25 km<sup>2</sup> is not high enough to resolve the fine-scale vertical gradients  
 290 around mountain slopes. On average, the depth of the GEOS-CF model surface layer is 130  
 291 meters and we use this value without attempting to adjust for sub-grid vertical gradients (Travis  
 292 et al., 2019). All aerosol evaluation is based on the GEOS-Chem aerosols, and model PM<sub>2.5</sub> is  
 293 calculated for a relative humidity (RH) of 35%. The validation covers the time period from the  
 294 start of the GEOS-CF data record on Jan 1, 2018 to Dec 31, 2019.

295  
 296 Figure 2 shows the global distribution of all in-situ observations used in the evaluation.  
 297 The GAW observation sites are located away from the major pollution sources, representing the  
 298 global background concentrations. In contrast, most observations available on the OpenAQ  
 299 platform are located in densely populated areas, providing information about local air pollution.  
 300 For our analysis, we only include OpenAQ locations with at least 80% of data coverage during  
 301 the 2-year period. The OpenAQ and AERONET observations are further grouped into six  
 302 geographical regions, as shown in Figure 2. This subset of observations provides good coverage  
 303 for North America, Europe, and Eastern Asia (especially China) but a limited view of other

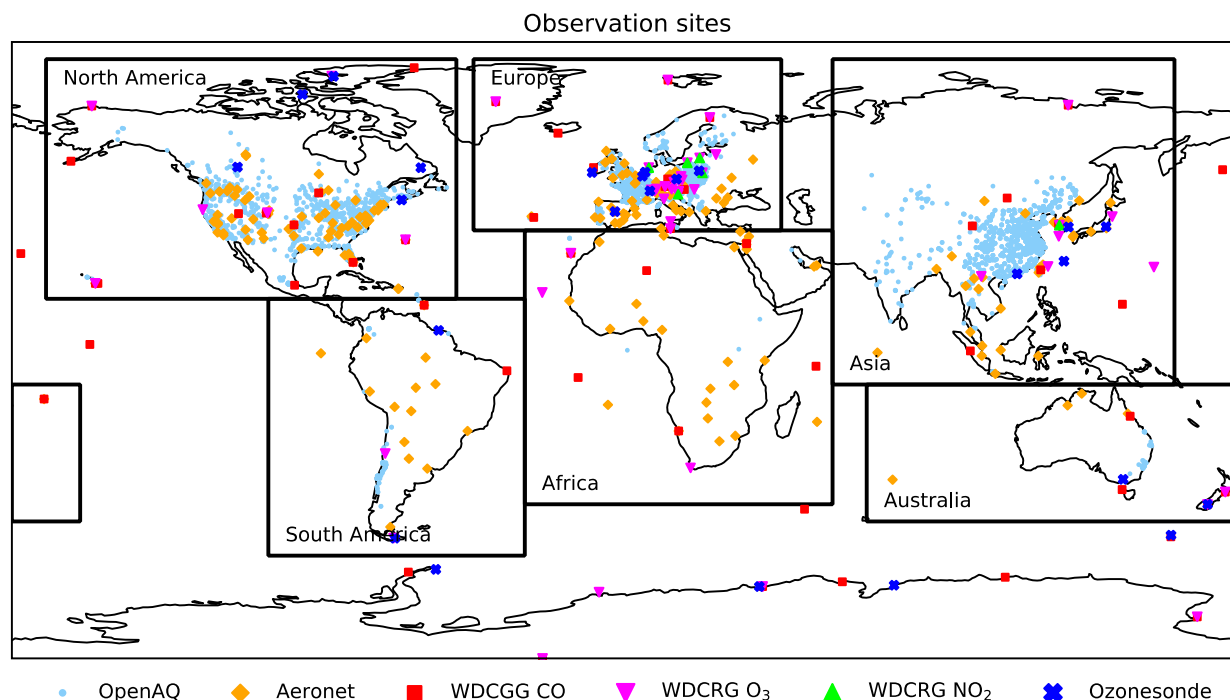
304 regions such as South America or Africa. For those under-represented regions, our analysis relies  
 305 heavily on the global daily satellite observations.

306

307 **Table 2.** Overview of observation data sets used for GEOS-CF model validation

Description	Species	# sites	Reference
Ozonesonde	O <sub>3</sub>	24	Thompson et al., 2017
NASA OMI NO <sub>2</sub> v4.0	Tropospheric NO <sub>2</sub>	global	Lamsal et al., 2020
MOPITT v8	Total CO	global	Deeter et al., 2019
AERONET	AOD at 550nm	195	Giles et al., 2019
GAW WDCGG	CO	54	<a href="https://gaw.kishou.go.jp/">https://gaw.kishou.go.jp/</a>
GAW WDRCG	O <sub>3</sub> , NO <sub>2</sub>	48 (O <sub>3</sub> ), 6 (NO <sub>2</sub> )	<a href="https://www.gaw-wdcr.org/">https://www.gaw-wdcr.org/</a>

308



309

310 **Figure 2.** Overview of observation sites used for model validation. Black boxes show the six  
 311 regions used for aggregation of OpenAQ and Aeronet observations.

## 312 4 Evaluation of Model Analysis

### 313 4.1. Model Skill Scores

314 We first highlight the model skill scores against all surface observations before  
 315 discussing the individual species in more detail below. Figure 3 shows monthly model skill  
 316 scores for O<sub>3</sub>, NO<sub>2</sub>, CO, and PM<sub>2.5</sub> and/or AOD, aggregated by observation type. The skill scores

317 used are the normalized mean bias (NMB), normalized root mean square error (NRMSE), and  
 318 Pearson correlation coefficient (R):

$$319 \quad NMB = \frac{\sum_{n=1}^N (y_n - o_n)}{o} \quad (1)$$

$$320 \quad NRMSE = \frac{\sqrt{\frac{1}{N} \sum_{n=1}^N (y_n - o_n)^2}}{o_{0.95} - o_{0.05}} \quad (2)$$

$$321 \quad R = \frac{\sum_{n=1}^N (y_n - \bar{y})(o_n - \bar{o})}{\sqrt{\sum_{n=1}^N (y_n - \bar{y})^2} \sqrt{\sum_{n=1}^N (o_n - \bar{o})^2}} \quad (3)$$

322 where  $y_n$  denotes an individual model estimate,  $\bar{y}$  is the model average,  $o_n$  is the observation  
 323 associated with  $y_n$ , and  $\bar{o}$  is the observation average;  $o_{0.05}$  and  $o_{0.95}$  are the 5th and 95th percentile,  
 324 respectively, of the observations sample, and  $N$  is the total number of hourly observation-model  
 325 pairs.

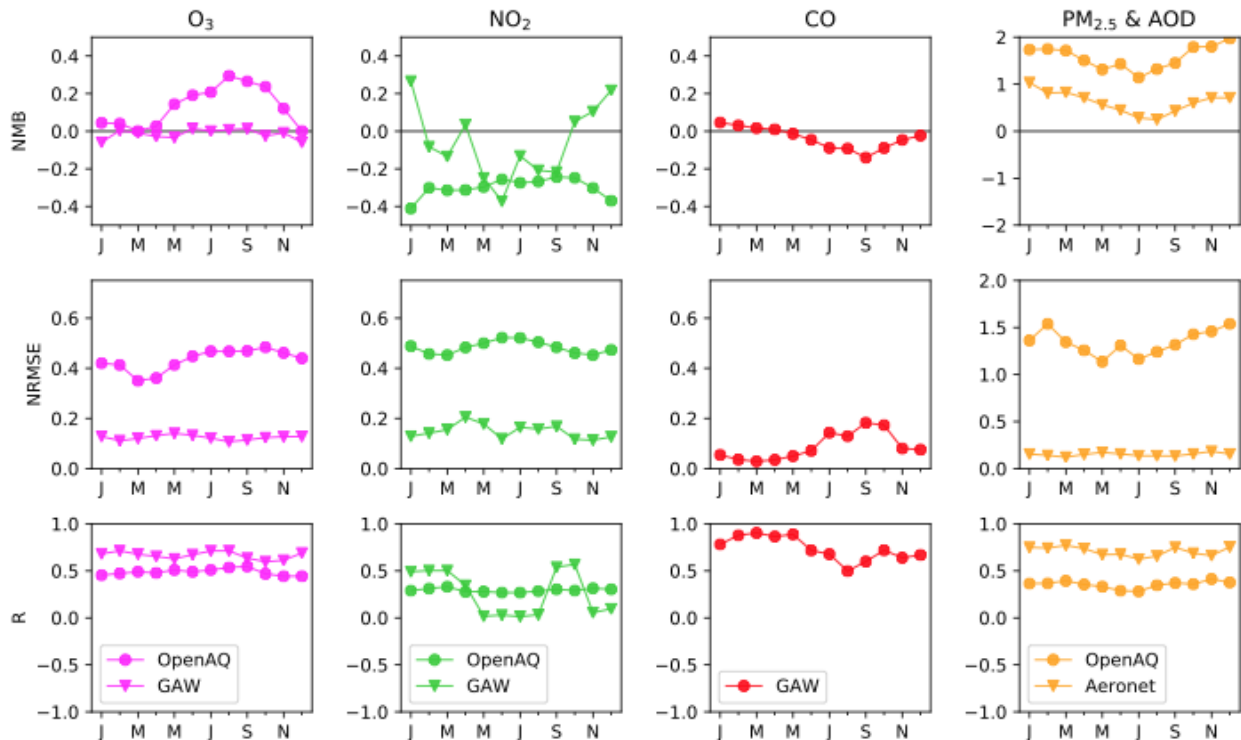
326 For hourly average surface  $O_3$ , the model shows a normalized mean annual bias of -0.015  
 327 compared to the GAW sites, with little seasonal variability (Figure 3). The GAW sites are  
 328 typically located in remote locations and the small model bias indicates that the model  
 329 adequately captures atmospheric background  $O_3$  throughout the year. This is confirmed by the  
 330 low NRMSE of 0.12 and the correlation coefficient of 0.66, again with small seasonal variability.  
 331 Compared to the GAW sites, the simulated  $O_3$  shows weaker skill scores relative to the OpenAQ  
 332 observations with an NMB of 0.13, an NRMSE of 0.43 and R of 0.49. As further discussed  
 333 below, the OpenAQ comparisons highlight a pronounced model overestimation of surface  $O_3$   
 334 during the summer months, especially over North America.

335 For  $NO_2$  (second column of Figure 3), the normalized model bias is -0.06 compared against the  
 336 GAW sites, and -0.30 against the OpenAQ sites. The model shows a strong seasonal change in  
 337 the NMB at the GAW sites, where the model on average overpredicts wintertime  $NO_2$  by up to  
 338 30% but underpredicts spring and early summer concentrations by a similar amount. The  
 339 OpenAQ bias shows the opposite direction with a reduction of the negative bias from -0.4 during  
 340 winter to -0.25 during summer. The NRMSE is 0.15 at the GAW sites and 0.48 at the OpenAQ  
 341 sites, similar to  $O_3$ . The R values for  $NO_2$  are the lowest for all analyzed species, with an average  
 342 score of 0.27 and 0.29 at the GAW and OpenAQ sites, respectively. Apart from potential  $NO_2$   
 343 observation interference with other nitrogen compounds (Winer et al., 1974; Grosjean and  
 344 Harrison, 1985; Steinbacher et al., 2007), we attribute this to the short atmospheric lifetime of  
 345  $NO_2$ , which makes it challenging for the model to capture the hourly variability in surface  $NO_2$   
 346 in full detail.

347 The simulated CO compares well against the 54 GAW sites, with an NMB of -0.036, an NRMSE  
 348 of 0.088 and R of 0.74. The model error is largest during the NH summer months, with a  
 349 decrease in NMB to -0.14, an increase in NRMSE to 0.18, and a reduction of R to 0.5.

350 The model comparisons against AERONET AOD and OpenAQ  $PM_{2.5}$  observations reveal a  
 351 systematic model overestimation of aerosol concentrations in GEOS-CF, with an average NMB  
 352 of 0.61 for AOD and 1.6 for surface  $PM_{2.5}$ . Known model issues in the treatment of model  
 353 emissions and wet scavenging contribute to these biases, as will be discussed in more detail  
 354 below. In addition, some  $PM_{2.5}$  observations on the OpenAQ platform represent dry particulate  
 355 matter while model  $PM_{2.5}$  assumes 35% RH, which also contributes to the mismatch. At the  
 356 AERONET sites, the model shows a good correlation score of 0.71 and the NRMSE of 0.15 is  
 357 comparable to that of other species at background sites, indicating that the model captures the  
 358  
 359  
 360

361 relative changes in AOD well despite the high model bias. For surface  $\text{PM}_{2.5}$ , the average model  
 362 NRMSE is 1.34 and R skill score is 0.35.  
 363



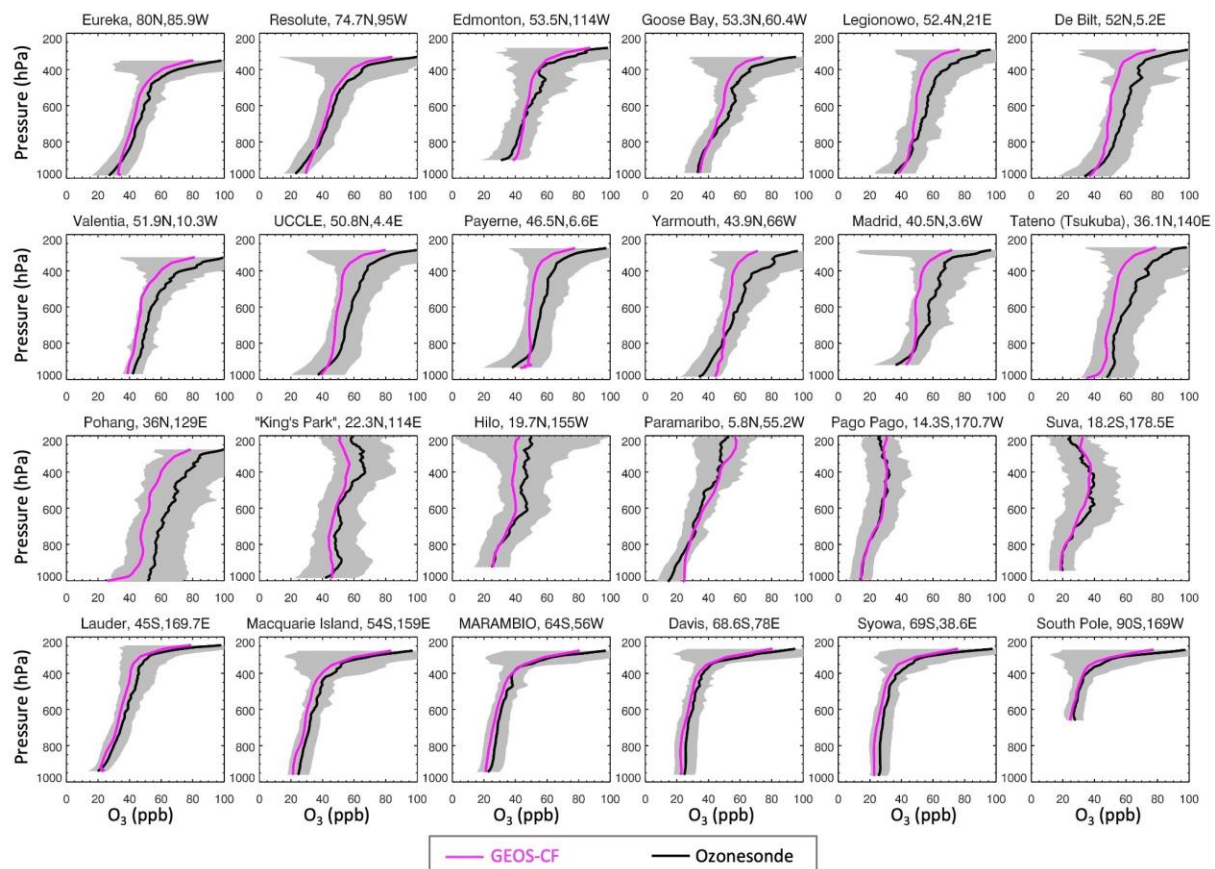
364  
 365 **Figure 3.** Overview of NMB, NRMSE and R for  $\text{O}_3$ ,  $\text{NO}_2$ ,  $\text{CO}$ , and  $\text{PM}_{2.5}$  (OpenAQ only) and  
 366 AOD (Aeronet only). Shown are the monthly skill score means aggregated by observation type.  
 367 Note the different scale for  $\text{PM}_{2.5}$  and AOD.

#### 368 4.2. Ozone

369 Comparisons of GEOS-CF against ozonesondes and GAW surface observations show  
 370 that GEOS-CF reproduces well-known features of background surface ozone, such as the local  
 371 maxima in the Northern Hemisphere (NH) during spring.

372 Figure 4 shows annual mean (2018-2019) vertical ozone profiles as observed by  
 373 ozonesondes at 24 locations across the world (see Figure 2 for locations), compared against  
 374 corresponding GEOS-CF model concentrations. While GEOS-CF generally captures the  
 375 observed vertical structure of ozone, the model tends to underestimate free tropospheric ozone  
 376 (approx. 800-300 hPa) over the NH midlatitudes. For these profiles (e.g., De Bilt, Payerne,  
 377 Madrid, Tateno), the simulated vertical gradient is much less pronounced than observed and the  
 378 model consistently underestimates ozone concentrations. This pattern is consistent with previous  
 379 comparisons of the online GEOS-Chem module against observations (Hu et al., 2018) and  
 380 implies two potential model errors: (1) excessive vertical mixing resulting in an overestimation  
 381 in the lower altitudes and underestimation at higher altitudes, as evident over Payerne,  
 382 Yarmouth, and Madrid (Figure 4); and (2) an underestimation of lightning  $\text{NO}_x$  over the NH  
 383 midlatitudes, resulting in an underestimation of ozone production in the upper troposphere. The  
 384 global lightning  $\text{NO}_x$  source in GEOS-CF is  $5.9 \text{ Tg N yr}^{-1}$ , in good agreement with other studies  
 385 (Schumann and Huntrieser, 2007) and the  $6.0 \text{ Tg N yr}^{-1}$  reported for the GEOS-Chem CTM  
 386 (Murray et al., 2012). However, due to the real-time nature of the system, the GEOS-CF

387 lightning parameterization uses the unconstrained cloud top height parameterization (Price and  
 388 Rind, 1992; 1993; 1994) and does not apply time-dependent, regional redistribution factors based  
 389 on Lightning Imaging Sensor (LIS) and the Optical Transient Detector (OTD) satellite  
 390 observations as is standard in GEOS-Chem. As described in Murray et al. (2012), this results in  
 391 an underestimation of simulated lightning flash rates over the Northern extratropics, which is  
 392 likely one of the main reasons for the model underestimation of ozone in the NH upper  
 393 troposphere. We also note that the model vertical resolution is approx. 500m (20 hPa) in the mid-  
 394 to upper troposphere, which might be insufficient to resolve the strong vertical gradients across  
 395 the tropopause boundary and contribute to the model-observation mismatches in the upper  
 396 troposphere. Over the Southern Hemisphere (SH), the simulated ozone profiles are in good  
 397 agreement with the ozonesonde observations and show an improved O<sub>3</sub> distribution compared to  
 398 the offline GEOS-Chem model (Hu et al., 2018).  
 399



400  
 401 **Figure 4.** Vertical profile of annual average ozone (2018-2019) at 24 sites as observed by  
 402 ozonesondes (black) and simulated by GEOS-CF (magenta). The grey shaded area indicates  
 403 sonde observation standard deviation.  
 404

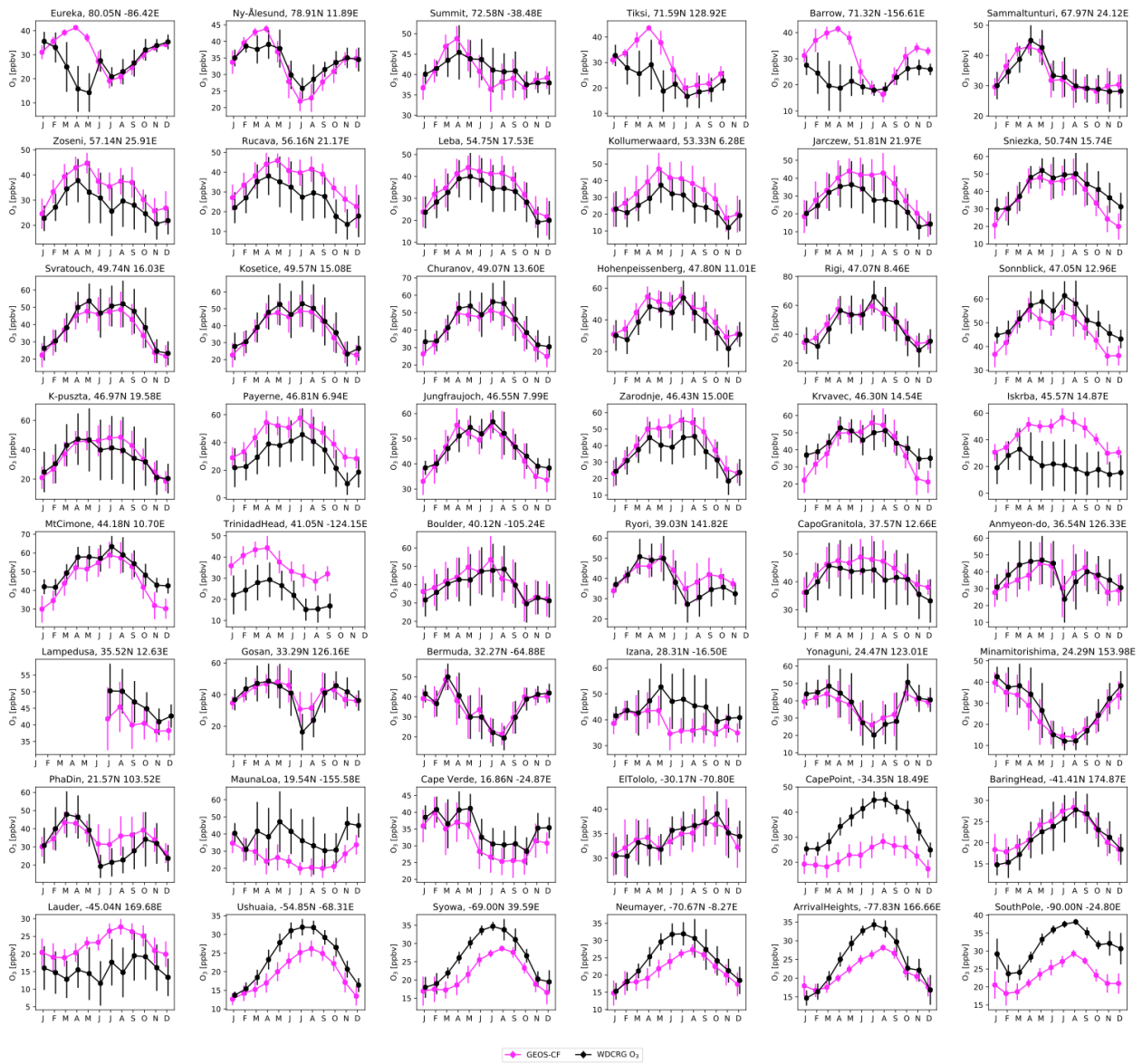
405 The GAW observations show a pronounced seasonal cycle for surface O<sub>3</sub> with a  
 406 maximum of 30-50 ppbv during spring and summer and a low of 10-30 ppbv in winter, a feature  
 407 that is well reproduced by GEOS-CF (Figure 5). At remote locations such as the high-latitude  
 408 GAW sites (Figure 5 top row), the seasonal cycle is more distinct with a peak in early spring.  
 409 The ozone maximum develops more slowly at locations that are more heavily influenced by  
 410 anthropogenic emissions. As already observed in the ozonesondes, the model underestimates

411 ozone over the Southern Ocean by up to 10 ppbv. This is likely due to excessive ozone  
412 deposition over seawater (Pound et al., 2020), a problem since corrected in newer versions of  
413 GEOS-Chem.

414

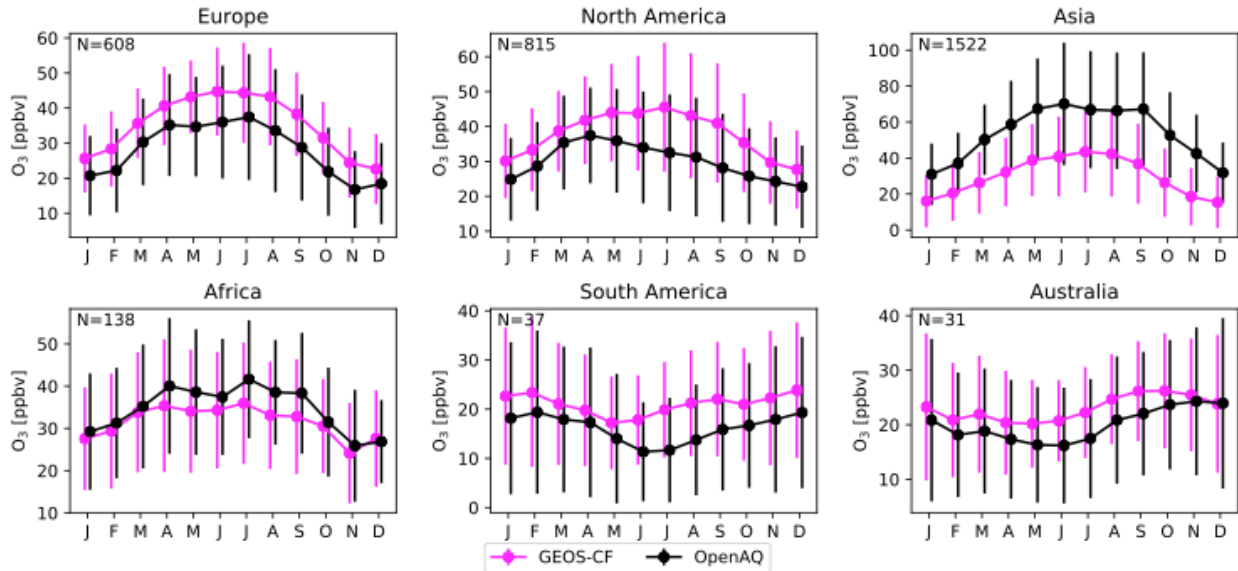
415 Figure 6 shows monthly average surface ozone by region, as captured by observations in  
416 the OpenAQ database and simulated by GEOS-CF. The model generally overestimates surface  
417 O<sub>3</sub> over Europe, North and South America and Australia by 5-10 ppbv and underestimates it over  
418 Africa and Asia by up to 20 ppbv. The model-observation mismatch is larger than for the remote  
419 GAW sites, suggesting that sub-grid factors such as vertical and horizontal model representation  
420 errors and nighttime loss of ozone by reaction with NO contribute to this difference (Travis et al.,  
421 2019; Dacic et al., 2020). Models generally underestimate ozone nighttime depletion (Travis et  
422 al., 2017) and evaluation of surface ozone is thus often restricted to daytime ozone (Hu et al.,  
423 2018, Travis et al., 2019). As shown in Figure 7, restricting the analysis to daytime ozone (12:00  
424 to 16:00 local time) does indeed improve the comparison and reduce the bias by up to 5 ppbv, in  
425 particular over Europe, South America and Australia. The model still shows a systematic  
426 positive bias over the US during summer and fall, a known issue in GEOS-Chem (Travis et al.,  
427 2017, Hu et al., 2018).

428 Factors that likely contribute to the high NH surface ozone in GEOS-CF are uncertainties in the  
429 production of ozone from the oxidation of isoprene (Travis et al., 2016; Bates et al., 2019) and  
430 errors in ozone deposition to wet surfaces (Travis et al., 2019). In addition, most OpenAQ  
431 observation sites are located near densely populated areas, and the 25x25 km<sup>2</sup> model simulation  
432 cannot fully capture the fine-scale features characteristic for these environments (Keller et al.,  
433 2020).

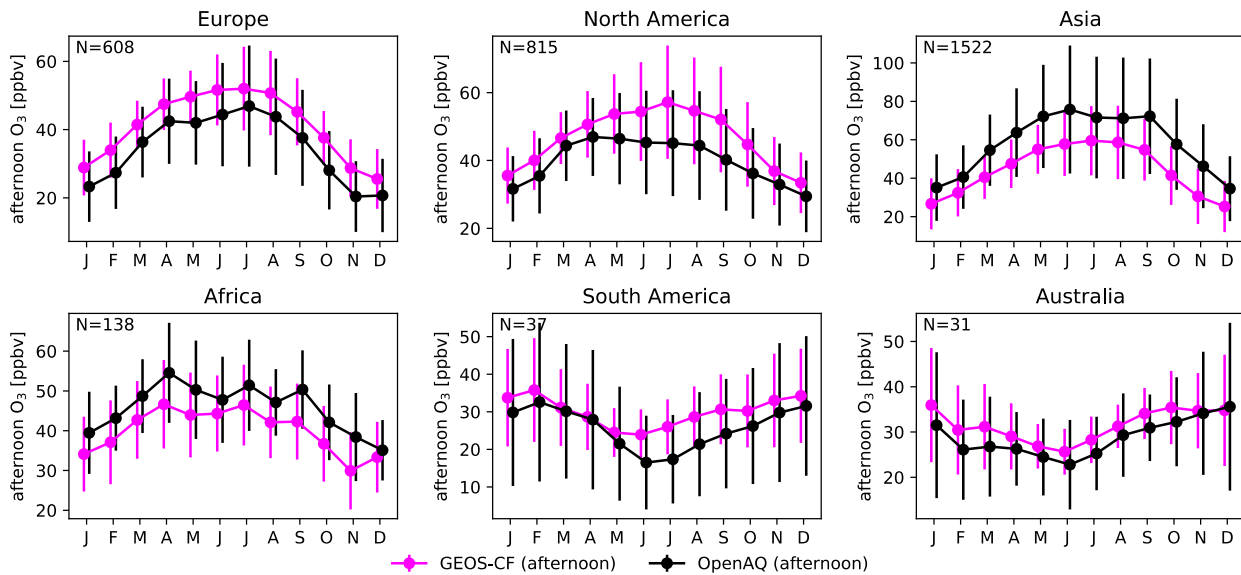


434  
435  
436  
437

**Figure 5.** Monthly average surface  $O_3$  as observed at 48 GAW sites (black) and simulated by GEOS-CF (magenta). Vertical bars represent the standard deviation of hourly variability. Y-axis ranges vary by station.



438  
 439 **Figure 6.** Monthly average surface  $O_3$  grouped into six regions as obtained from the OpenAQ  
 440 database (black) and simulated by GEOS-CF (magenta). Vertical bars represent the standard  
 441 deviation of hourly variability across all sites. Number of sites is given in the inset. Y-axis ranges  
 442 vary by region.  
 443



444  
 445 **Figure 7.** As Figure 6 but using afternoon ozone only (12:00-16:00 local time).  
 446

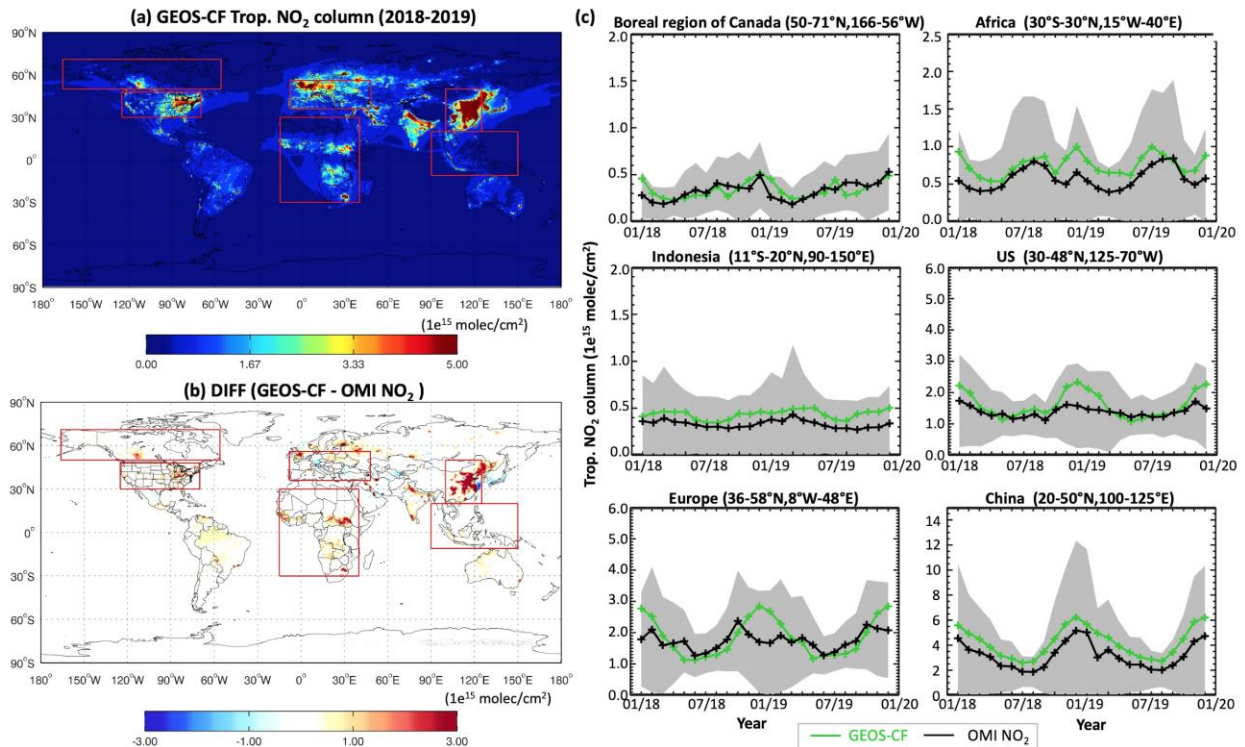
### 4.3. Nitrogen Dioxide

447 As shown in Figure 8, GEOS-CF captures major features of the global distribution of  
 448 tropospheric  $NO_2$ . The model simulated  $NO_2$  columns (Figure 8a) show distinct hot spots over  
 449 urban areas (Eastern China, Europe, Eastern US), reflecting the dominant contribution of fossil  
 450 fuel combustion coupled with the short atmospheric lifetime of  $NO_2$  (Streets et al., 2013, Duncan  
 451 et al., 2016). Additional hot spots resulting from biomass burning are found over Africa and the  
 452 boreal region of Canada (Figure 8a). The spatial pattern simulated by GEOS-CF agrees well with  
 453 the  $NO_2$  columns observed by OMI. Over Eastern China, the model simulated  $NO_2$  columns are

454 up to  $3.0 \times 10^{15}$  molecules  $\text{cm}^{-2}$  (or approx. 40%) higher than the OMI observations (Figure 8b),  
 455 suggesting a potential overestimation of  $\text{NO}_x$  emissions or a longer  $\text{NO}_x$  lifetime in the model  
 456 (Shah et al., 2020). However, the OMI retrieval algorithm v4.0 tends to underestimate  
 457 tropospheric  $\text{NO}_2$  over polluted areas (Lamsal et al., 2020), which complicates the analysis. As  
 458 further discussed in the next section, the comparison against surface observations does not  
 459 support the view of a broad-based overestimation of surface  $\text{NO}_2$  over Asia.

460 As shown in Figure 8c, the simulated seasonality of tropospheric  $\text{NO}_2$  columns is in good  
 461 agreement with OMI observations. Over areas dominated by anthropogenic activities, such as the  
 462 US, Europe, and China, the simulated  $\text{NO}_2$  columns show a distinct seasonal cycle with the  
 463 minimum during summer and peak during winter, driven by the seasonal variation in  $\text{NO}_x$   
 464 lifetime against oxidation (Shah et al., 2020). The seasonal cycle observed over China is well  
 465 captured by GEOS-CF, while the simulated wintertime peak over the US and Europe is higher  
 466 than observed by OMI. Chemical loss of  $\text{NO}_x$  during winter is dominated by  $\text{N}_2\text{O}_5$  hydrolysis,  
 467 which is sensitive to  $\text{NO}_x$  emissions and ozone concentrations (Jaeglé et al, 2018; Shah et al.,  
 468 2020). Over Africa, the seasonal cycle is dominated by summer biomass burning, which is well  
 469 captured by the model.

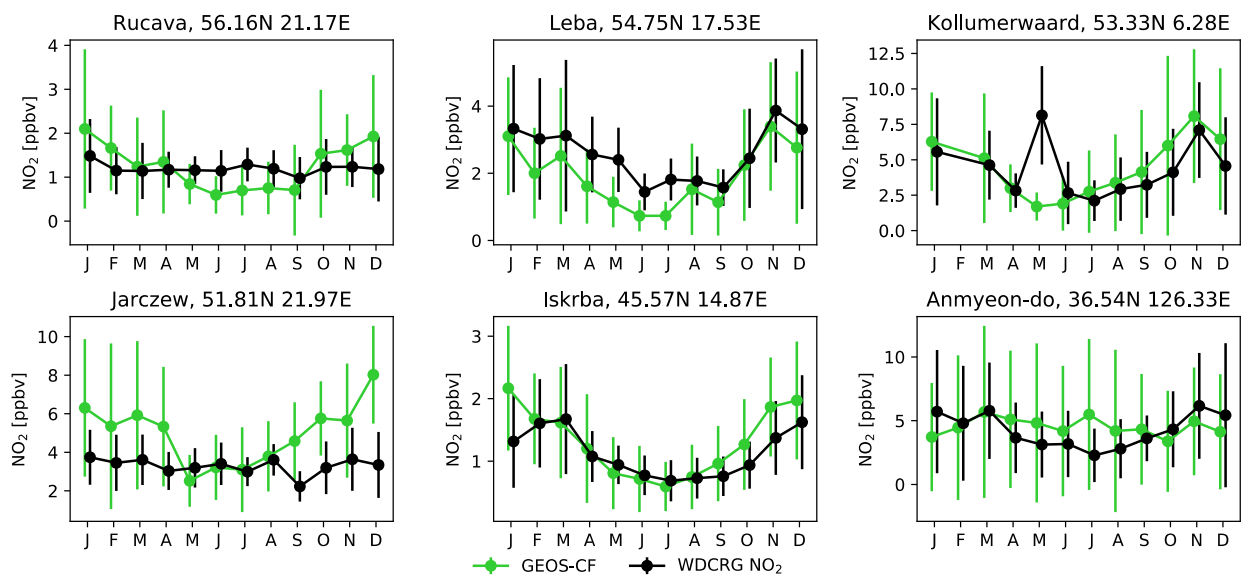
470



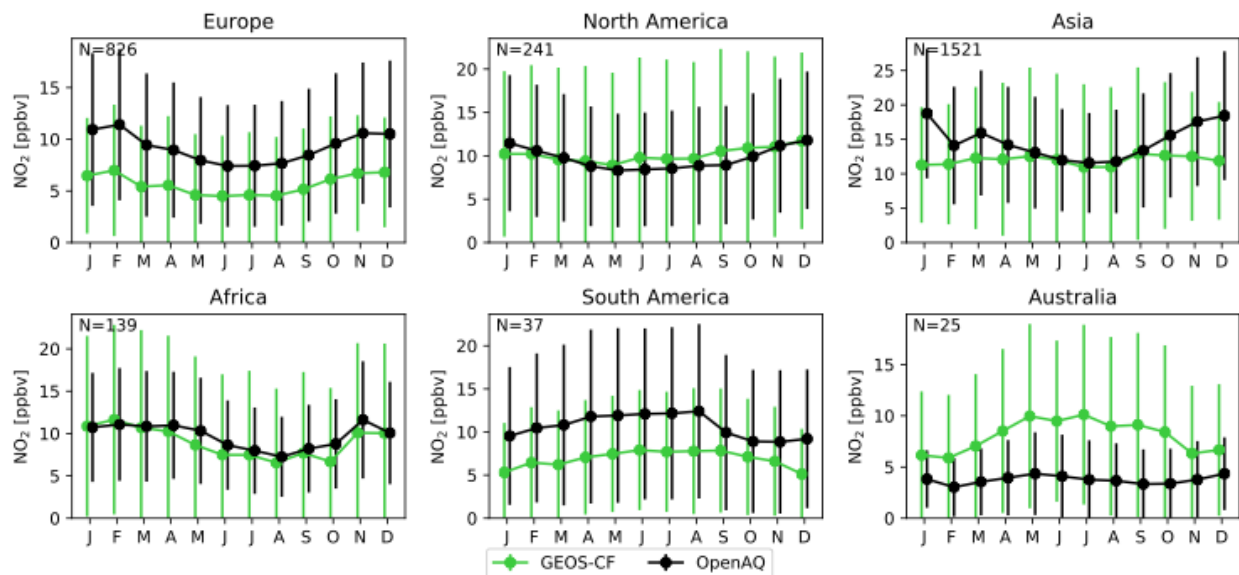
471 **Figure 8.** Comparison of GEOS-CF against OMI tropospheric column  $\text{NO}_2$ . **a)** the 2018-2019  
 472 average tropospheric  $\text{NO}_2$  column (1-2pm local time) as simulated by GEOS-CF. **b)** the  
 473 difference between model simulated tropospheric column and NASA OMI  $\text{NO}_2$  (v4.0)  
 474 observations. **c)** Right panel shows the tropospheric  $\text{NO}_2$  time series averaged for six regions, as  
 475 shown in **a** and **b** (n.b., y-axis intervals are not the same for each time-series).  
 476

477  
 478 Figure 9 shows comparisons of monthly mean surface  $\text{NO}_2$  at 6 GAW sites (n.b., all  
 479 located in Europe) against model simulated concentrations. These comparisons show that GEOS-  
 480 CF is in good agreement with the (non-mountainous) GAW sites, suggesting that it provides a

481 realistic simulation of background surface  $\text{NO}_2$  over Europe. Figure 10 further evaluates the  
 482 simulated distribution of global surface  $\text{NO}_2$  in comparison to observations in OpenAQ. The  
 483 model is in excellent agreement with observations over North America and Africa but  
 484 underestimates concentrations over Europe and South America, as well as Asia during the  
 485 wintertime. The apparent low bias over Europe and Asia is inconsistent with the tropospheric  
 486 column comparisons shown in Figure 8 and also the comparison against the GAW observations  
 487 (Figure 9), which do not show such a systematic underestimation of  $\text{NO}_2$  by GEOS-CF.  
 488 The comparison of surface concentrations of  $\text{NO}_2$  is complicated by the fact that most surface  
 489 observations are based on chemiluminescence using a molybdenum converter, which can result  
 490 in an overestimation of reported  $\text{NO}_2$  concentrations due to interference with other oxidized  
 491 nitrogen compounds (Winer et al., 1974; Grosjean and Harrison, 1985; Steinbacher et al., 2007).  
 492 This might explain some of the model underestimation of  $\text{NO}_2$  relative to the OpenAQ  
 493 observations. In addition, since the OpenAQ observations tend to be located in relative proximity  
 494 to urban areas they often do not represent the regional average  $\text{NO}_2$  concentrations captured by  
 495 GEOS-CF, which can introduce a systematic bias. While this is an issue for all analyzed species,  
 496 the problem is particularly pronounced for  $\text{NO}_2$  given its large spatial and temporal variability.  
 497



498  
 499 **Figure 9.** Monthly average surface  $\text{NO}_2$  as observed at 6 GAW sites (black) and simulated by  
 500 GEOS-CF (green). Vertical bars represent the standard deviation of hourly variability. Y-axis  
 501 ranges vary by station.



502  
 503 **Figure 10.** Monthly average surface  $\text{NO}_2$  grouped into six regions as obtained from the OpenAQ  
 504 database (black) and simulated by GEOS-CF (green). Vertical bars represent the standard  
 505 deviation of hourly variability across all sites. Number of sites is given in the inset. Y-axis ranges  
 506 vary by region.

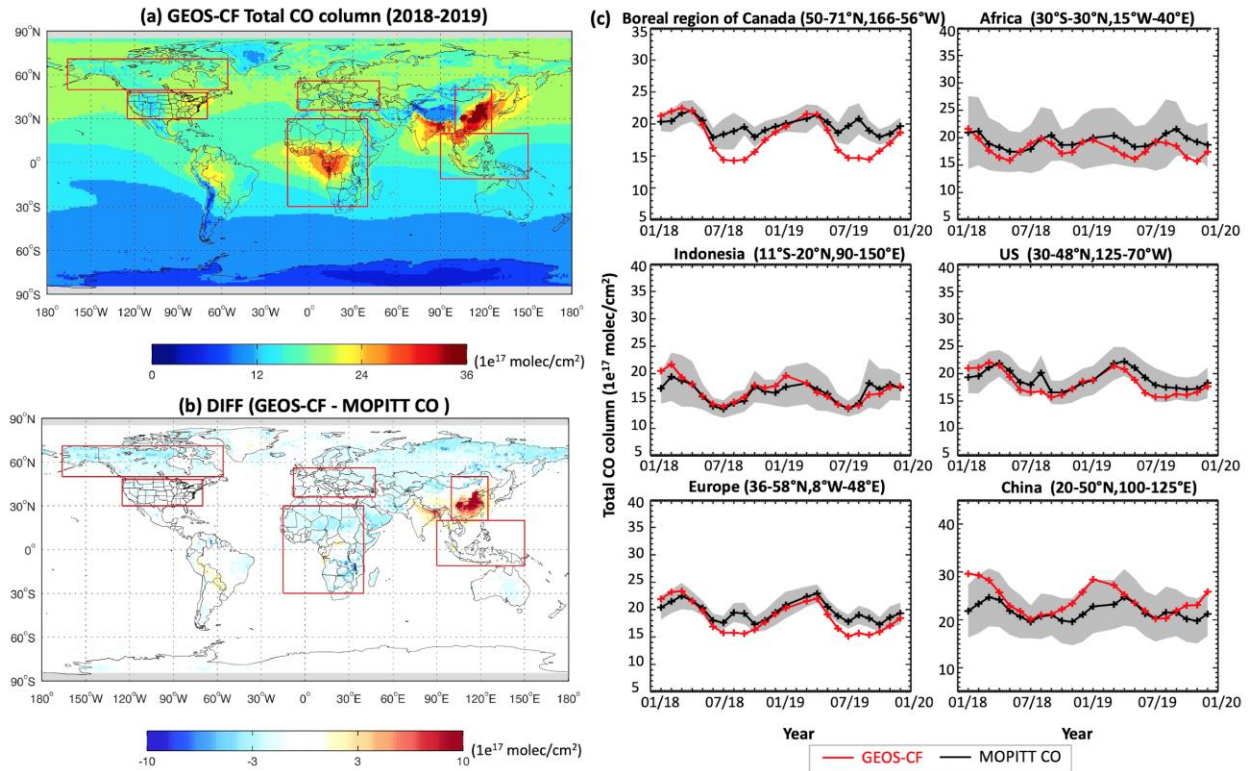
#### 507 4.4. Carbon Monoxide

508 Our analysis of simulated CO shows that the model has no significant global CO bias  
 509 compared against satellite and surface observations. Figure 11 shows the global distribution and  
 510 seasonal cycle of total column CO retrieved from MOPITT and derived from GEOS-CF. Local  
 511 MOPITT averaging kernels were applied to the GEOS-CF CO profiles to obtain the column  
 512 values. The model simulated CO pattern is in good agreement with MOPITT, with local maxima  
 513 over major polluted areas (East China, India) and over biomass burning regions (South America  
 514 and Central Africa). Similar to  $\text{NO}_2$ , the simulated CO columns over China are larger than the  
 515 observations, possibly due to an overestimation of CO emissions over that region. The baseline  
 516 anthropogenic CO emissions in GEOS-CF are scaled based on ODIAC emission trends, with  
 517 strongest increases over China and India (Oda et al., 2018). Our scaling methodology assumes a  
 518 constant CO/ $\text{CO}_2$  emissions ratio, and any decrease in the CO/ $\text{CO}_2$  emission ratio, e.g. due to a  
 519 technology shift, would result in an overestimation of CO emissions.

520 The seasonal cycle of CO is determined by its shorter chemical lifetime during summer  
 521 due to increased photochemical activity, which is reflected in lower NH concentrations during  
 522 July and August where the model underestimates the MOPITT concentrations in the NH middle  
 523 and high latitudes by 10-20% (Figure 11c). This underestimation is driven by a stronger than  
 524 observed decrease of simulated total column CO during summertime, a pattern that is confirmed  
 525 by comparisons against the GAW surface observations (Figure 12). While the model  
 526 underestimates summertime surface CO in the NH, the opposite is true for the SH where model  
 527 simulated concentrations during summer are higher than the observations. A low bias in CO is a  
 528 long-standing issue in atmospheric chemistry models, commonly attributed to an  
 529 underestimation of direct emissions and inconsistencies in the simulated distribution of the  
 530 hydroxyl radical OH, the main atmospheric oxidant (Shindell et al., 2006; Strode et al., 2015,  
 531 Flemming et al., 2015; Monks et al., 2015; Gaubert et al., 2016). The air mass-weighted mean

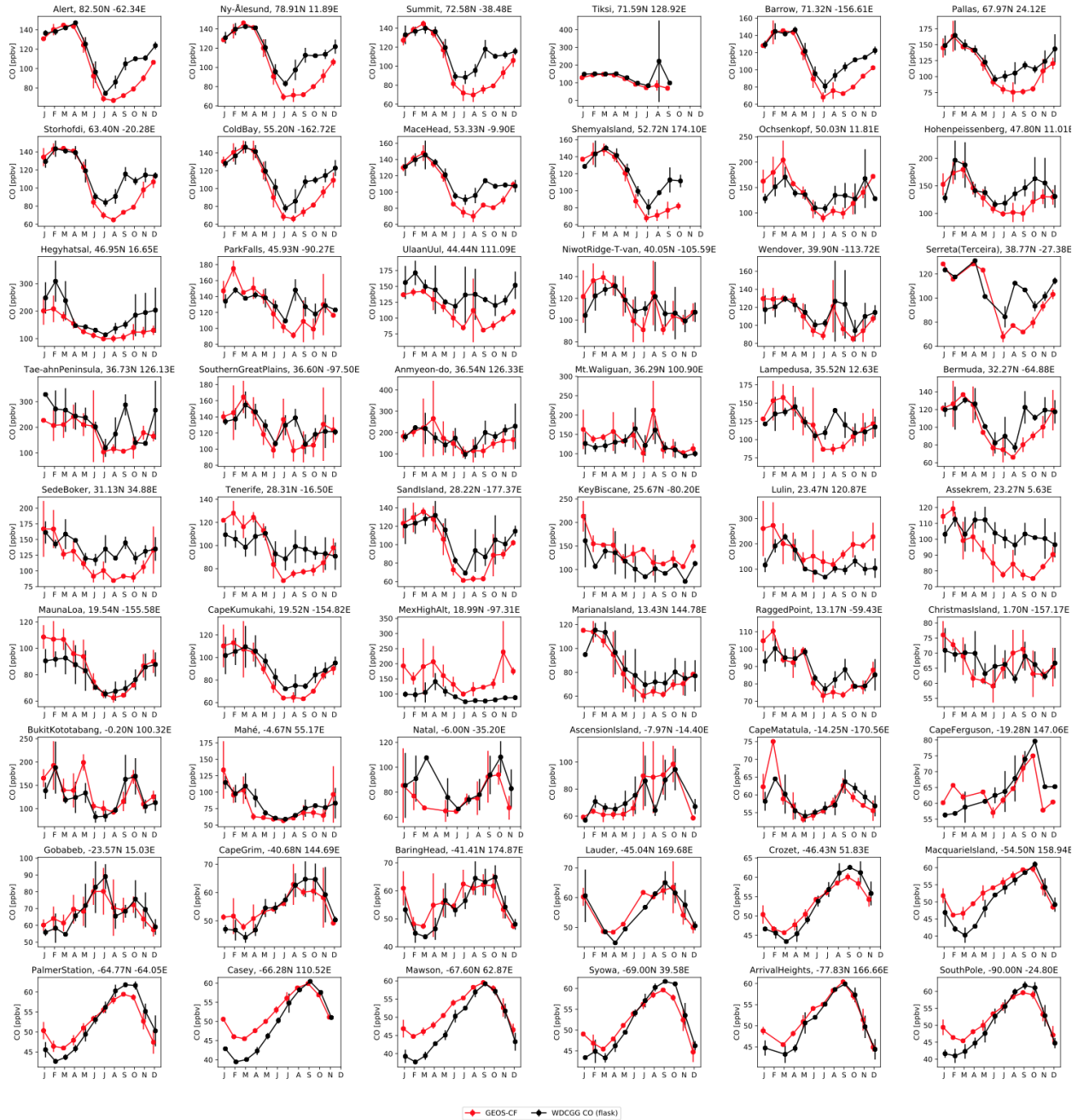
532 tropospheric OH in GEOS-CF is  $11.9 \times 10^5$  molecules  $\text{cm}^{-3}$ , in good agreement with other  
 533 models as well as estimates derived from methyl chloroform observations (Spivakovsky et al.,  
 534 2000; Montzka et al., 2000; Naik et al., 2013). The inter-hemispheric (NH/SH) ratio is 1.33,  
 535 again in good agreement with other model estimates (Naik et al., 2013) but higher than  
 536 observation-derived values of 0.8-1.0 (Montzka et al., 2000; Prinn et al. 2001; Krol and  
 537 Lelieveld 2003; Patra et al., 2014). This is consistent with an underestimation of summertime CO  
 538 in the northern high-latitudes - as shown by the comparisons against MOPITT and the GAW  
 539 surface observations (Figures 11 and 12) - and an overestimation of SH CO (Figure 12). An  
 540 overestimation of NH OH in GEOS-CF is also supported by inversion studies using the GEOS-  
 541 Chem CTM, which find that a similar OH correction is needed to match methane observations  
 542 (Zhang et al., 2020).

543



544

545 **Figure 11.** Comparison of GEOS-CF against MOPITT V8 total column CO. Top left panel  
 546 shows the 2018-2019 average total CO column as simulated by GEOS-CF. Bottom left panel  
 547 shows the difference between model simulated total column and MOPITT observations. Right  
 548 panel shows the total CO time series averaged for six regions, as shown on the left.



549  
 550 **Figure 12.** Monthly average surface CO as observed at 54 GAW sites (black) and simulated by  
 551 GEOS-CF (red). Vertical bars represent the standard deviation of hourly variability. Y-axis  
 552 ranges vary by station.

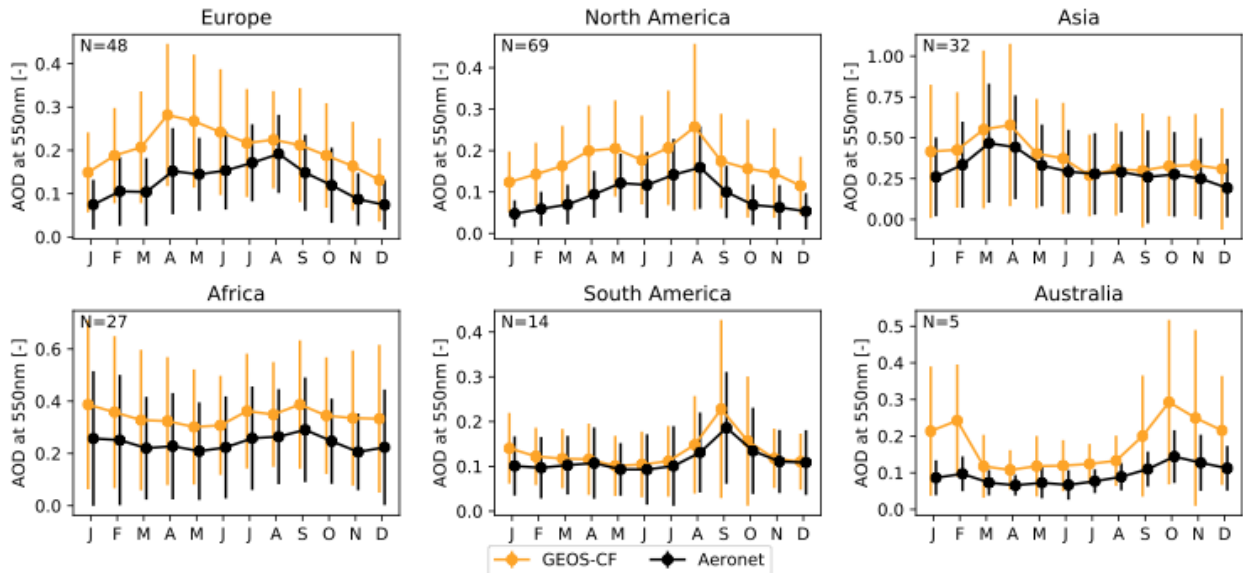
553 **4.5. Aerosols**

554 The evaluation of model simulated O<sub>3</sub>, NO<sub>2</sub> and CO has shown that GEOS-CF  
 555 reproduces many of the features of the tropospheric distribution of these trace gases. With  
 556 respect to aerosols simulated by GEOS-Chem, our validation shows that GEOS-CF has a high  
 557 bias but still captures many of the observed spatial and temporal patterns. A high bias in aerosols  
 558 is a known issue in GEOS-Chem v12.0.1 used in GEOS-CF v1.0, and recent versions of GEOS-

559 Chem show improved simulation of aerosols including surface PM<sub>2.5</sub> (Luo et al., 2019; 2020;  
 560 Carter et al., 2020).

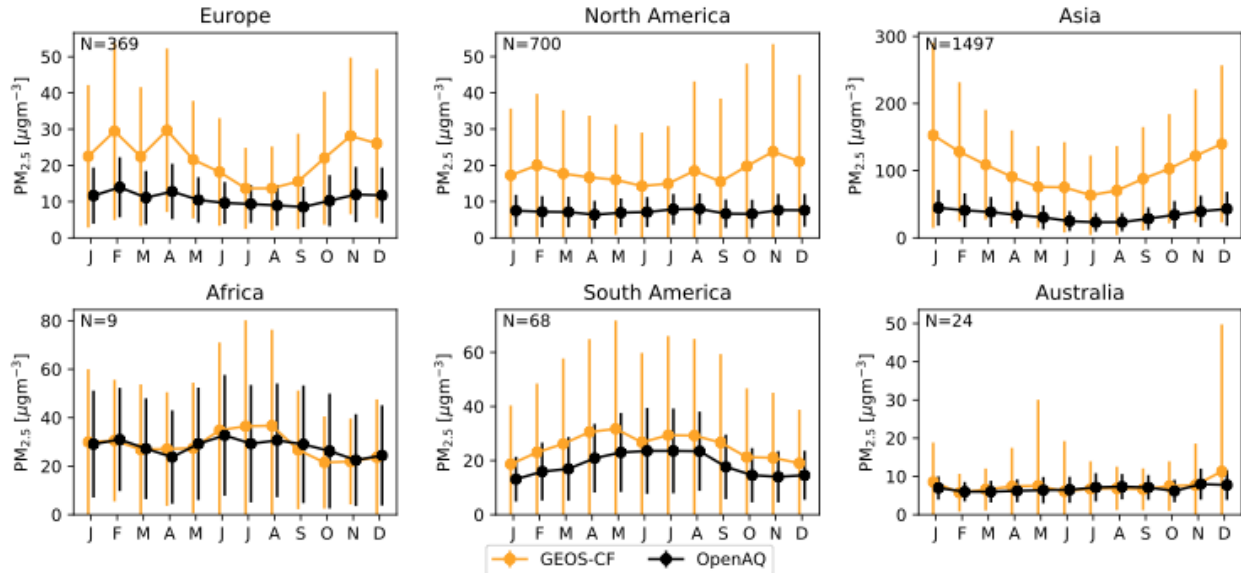
561 Figure 13 compares model simulated AOD at 550nm against AERONET observations,  
 562 and Figure 14 shows corresponding model-observation comparisons for surface PM<sub>2.5</sub>. GEOS-  
 563 CF overestimates the observations for both AOD and surface PM<sub>2.5</sub>, pointing toward a systematic  
 564 overestimation of aerosols in the model. On a relative basis, the overprediction is most  
 565 pronounced for Europe and North America, and the largest absolute bias of surface PM<sub>2.5</sub> is  
 566 found over Asia. We attribute part of the model overestimation to inadequate treatment of wet  
 567 scavenging processes, which results in an overprediction of aerosol nitrate and ammonium,  
 568 especially over Asia (Luo et al., 2019; 2020). Further, the QFED biomass burning emissions  
 569 inventory uses enhancement factors based on the GOCART model to better match MODIS-  
 570 observed AOD (Darmanov and Da Silva, 2015), which results in an overestimation of biomass  
 571 burning emissions if the differences between the GEOS-Chem and GOCART aerosol  
 572 parameterizations are not accounted for (Carter et al., 2020).

573



574

575 **Figure 13.** Monthly average Aerosol optical depth (AOD) at 550nm grouped into six regions as  
 576 observed at AERONET sites (black) and simulated by GEOS-CF (orange). Vertical bars  
 577 represent the standard deviation of daily variability. Number of sites is given in the inset. Y-axis  
 578 ranges vary by region.



579  
 580 **Figure 14:** Monthly average surface  $\text{PM}_{2.5}$  grouped into six regions as obtained from the  
 581 OpenAQ database (black) and simulated by GEOS-CF (orange). Vertical bars represent the  
 582 standard deviation of hourly variability. Number of sites is given in the inset. Y-axis ranges vary  
 583 by region.

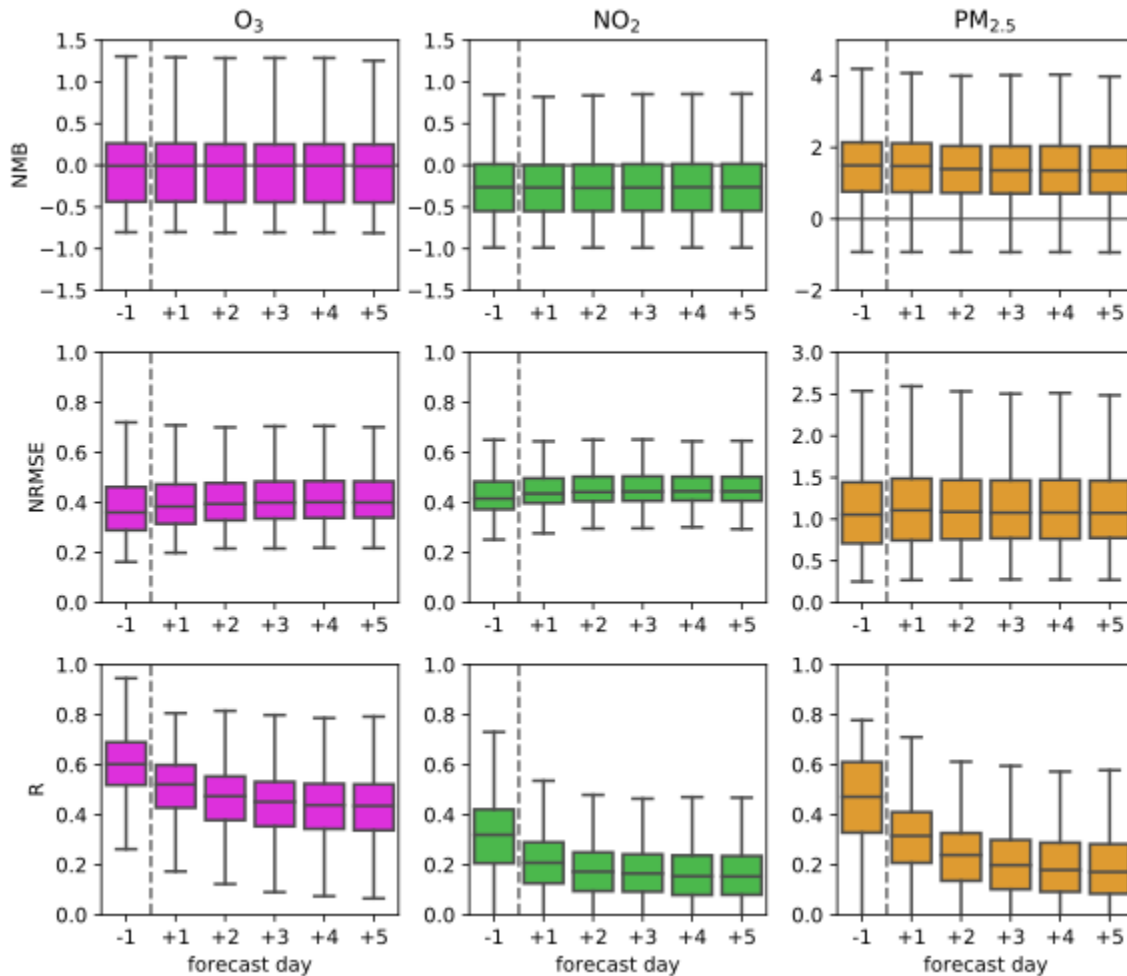
## 584 5 Evaluation of Model Forecasts

### 585 5.1. Comparison of Model Forecasts against Observations

586 GEOS-CF v1.0 does not directly assimilate trace gas observations and differences  
 587 between the 1-day analysis and the model forecasts are thus mainly driven by variations between  
 588 the forecasted and analyzed meteorological state. The meteorology not only impacts the flow of  
 589 the constituents but also affects deposition and dynamically calculated emissions, including  
 590 lightning  $\text{NO}_x$ , biogenic VOCs, sea salt aerosols, and dust (see Table 1). Further, the model  
 591 forecasts assume persistence in the biomass burning emissions, meaning the fires observed  
 592 during the analysis are assumed to continue burning and emitting the same amount for the next  
 593 five days. The model thus does not capture changes in occurrence or intensity of wildfires, both  
 594 of which can lead to significant changes in surface air pollution close to and downwind from the  
 595 fires.

596 Figure 15 shows model-observation skill scores for the model analysis (forecast day -1)  
 597 and the 5-day forecasts (forecast days +1 to +5) for  $\text{O}_3$ ,  $\text{NO}_2$ , and  $\text{PM}_{2.5}$ . The results for the  
 598 analysis are the same as discussed in Section 4 (Figure 3). Skill scores were calculated at each  
 599 observation site individually before aggregating them in the form of boxplots, as shown in Figure  
 600 15. For all three evaluated species, the model analysis showed the best agreement with the  
 601 observations. The median NMB of the model analysis is -0.01 for  $\text{O}_3$ , -0.26 for  $\text{NO}_2$ , and 1.50 for  
 602  $\text{PM}_{2.5}$ , with almost no difference between the analysis and the model forecasts. Relative to the  
 603 analysis, the forecasted NRMSE and R become incrementally worse for the 1-day to 3-day lead  
 604 forecasts, while there is little further deterioration between the 3-day forecasts and the 5-day  
 605 forecasts. The median NRMSE is 0.36 for  $\text{O}_3$ , 0.42 for  $\text{NO}_2$  and 1.05 for  $\text{PM}_{2.5}$ . The NRMSE  
 606 slightly deteriorates with increasing forecast lead time, resulting in NRMSE's for the 5-day  
 607 forecast of 0.4 for  $\text{O}_3$ , 0.45 for  $\text{NO}_2$  and 1.07 for  $\text{PM}_{2.5}$ . This indicates that errors in the

608 meteorological forecasts (and biomass burning emissions) indeed impact the quality of the  
 609 surface air quality forecasts. The increase in NRMSE is most pronounced for  $O_3$ , whose  
 610 chemistry is strongly controlled by meteorological factors such as solar radiation, temperature,  
 611 and humidity (e.g., Jacob et al., 1993; Sillman and Samson, 1995, Tarasova and Karpetchko,  
 612 2003). The largest change in skill score between analysis and forecasts is found for R, which  
 613 drops from 0.6 for the analysis to 0.44 for the 5-day forecast for  $O_3$ , 0.32 to 0.15 for  $NO_2$ , and  
 614 0.47 to 0.17 for  $PM_{2.5}$ . Of the three analyzed skill scores, R is most sensitive to errors in the  
 615 temporal pattern and we attribute a large fraction in the deterioration in R to transport errors in  
 616 the forecasts, such as the evolution of frontal systems or the dispersion of smoke plumes.  $PM_{2.5}$   
 617 is particularly sensitive to these factors given its large spatiotemporal gradients, comparatively  
 618 long atmospheric lifetime, and strong sensitivity to changes in biomass burning emissions.



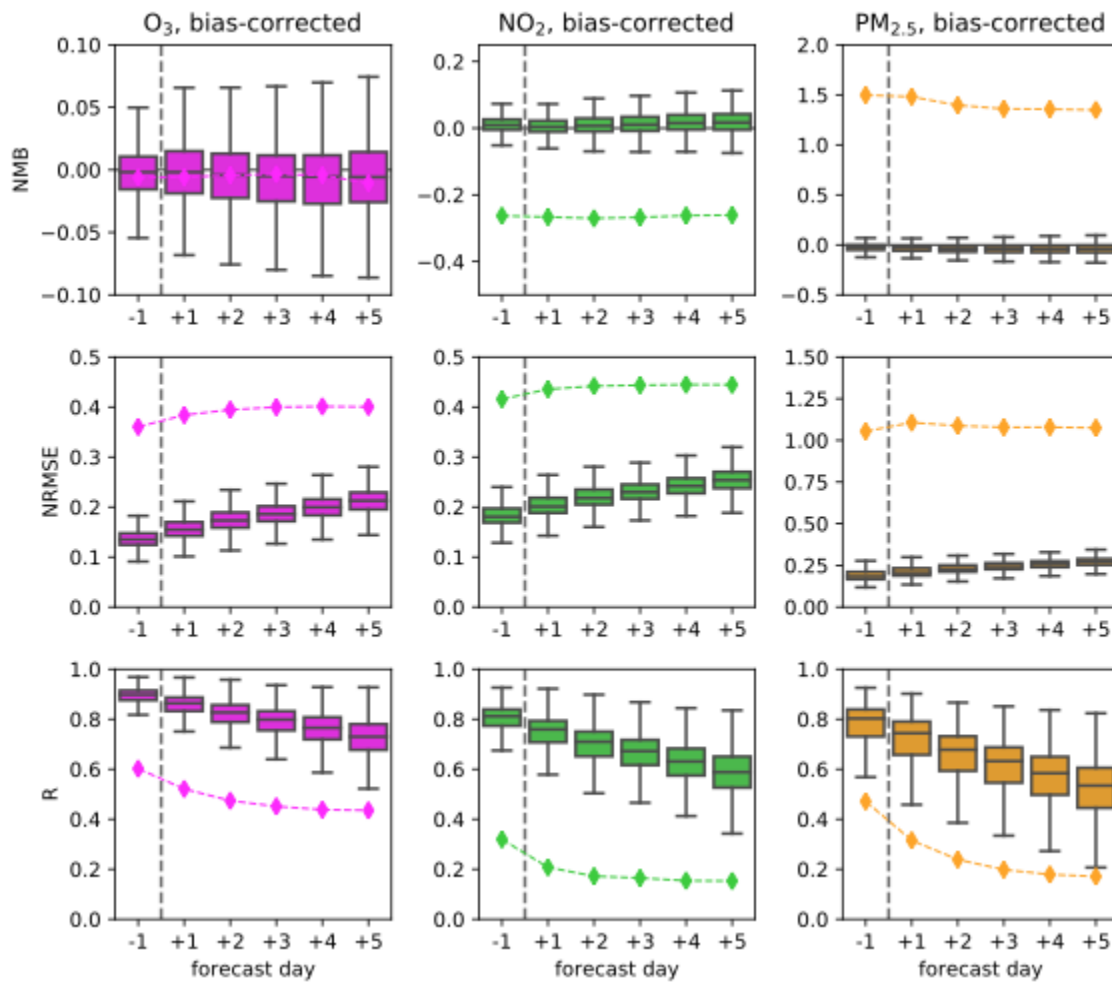
619  
 620 **Figure 15.** GEOS-CF model skill scores for the analysis (forecast day -1) and the 5-day forecasts  
 621 (forecast day +1 to +5) relative to surface observations. Boxplots show the variation in the NMB,  
 622 NRMSE, and R across all surface sites for  $O_3$ ,  $NO_2$ , and  $PM_{2.5}$ .

## 623 5.2. Bias-corrected Local Forecasts

624 As discussed above, model-predicted concentrations of  $O_3$ ,  $NO_2$  and  $PM_{2.5}$  can differ  
 625 from the observations for a number of reasons, including model representation errors,  
 626 uncertainties in the meteorology, or model biases arising from errors in the model treatment of

627 emissions, deposition, or atmospheric chemistry. One approach to deal with these issues is to  
 628 quantify and correct these systematic model errors in a post-processing step. Such bias correction  
 629 methods can be applied to near real-time model forecasts and have been found to be an effective  
 630 tool to significantly improve local model predictions, e.g., by using mean subtraction (McKeen  
 631 et al., 2005; Wilczak et al., 2006), historical analogs (Hamill and Whitaker, 2006), Kalman-  
 632 filtering (Delle Monache et al., 2006; Djalalova et al., 2015), or kriging (Honoré et al., 2008).  
 633 More recently, machine learning (ML) approaches have become popular to relate model output  
 634 to air quality observations (e.g., Grange et al., 2018; Grange and Carslaw, 2019; Ivatt and Evans,  
 635 2020; Petetin et al., 2020). As discussed in Keller et al. (2020), bias-correction using ML can  
 636 significantly reduce GEOS-CF model biases compared to surface observations. This is illustrated  
 637 in Figure 16, which shows the GEOS-CF model skill scores for the same data set analyzed in  
 638 Section 8 but using bias-corrected model concentrations instead of the original model output.  
 639 The bias correction methodology is described in detail in Keller et al. (2020). It uses the  
 640 XGBoost algorithm (Chen and Guestrin, 2016) to correct the original model predictions of  $O_3$ ,  
 641  $NO_2$ , and  $PM_{2.5}$  based on local meteorology and composition, as predicted by the GEOS-CF  
 642 model. The ML algorithm was trained on analysis data for year 2018 and the results shown in  
 643 Figure 16 are for year 2019.

644



645

646

647

**Figure 16.** Similar to Figure 14 but boxplots indicate the GEOS-CF model skill scores for the bias-corrected analysis (forecast day -1) and the bias-corrected 5-day forecasts (forecast day +1

648 to +5) relative to surface observations as boxplots and the median statistics of the non-corrected  
649 model values from Figure 15 shown as diamonds.

650

651 Compared to the uncorrected model output (indicated by the diamonds in Figure 16), the  
652 bias-corrected model values agree much better with the observations for all species, skill scores,  
653 and lead times. For all three species, the NMB of the bias-corrected values is close to zero for  
654 both the analysis and the 5-day forecasts. This result is not unexpected given that the ML  
655 algorithm is designed to minimize the model bias. The NRMSE and R scores are also  
656 significantly improved compared to the original data, with RMSE values of 0.1-0.2 and R values  
657 between 0.6-0.9 for the analysis. The skill scores of the bias-corrected forecasts deteriorate more  
658 rapidly than is the case for the uncorrected output but still outperform the original forecasts for  
659 all five lead days. Since the ML algorithm was only trained on the analysis data, model errors in  
660 the meteorology forecasts will also negatively impact the quality of the bias correction applied to  
661 the (forecast) baseline, which explains the steady decline in the skill scores for the bias-corrected  
662 forecasts.

## 663 **6 Conclusions**

664 The GEOS-CF system provides global, near real-time and 5-day forecast simulations of  
665 atmospheric composition and meteorology at the high global resolution of 0.25 degrees --  
666 including 5-day forecasts -- based on the GEOS-Chem chemistry module online within the  
667 GEOS GCM. Comparisons against a suite of satellite, ozonesonde and surface observations  
668 demonstrate that the model realistically captures the global distribution of a wide range of air  
669 constituents, including O<sub>3</sub>, NO<sub>2</sub>, and CO. For these three species, the model shows little biases at  
670 background locations, with NMB values ranging between -0.1 to +0.1. Like other atmospheric  
671 chemistry models, the model overestimates surface ozone in the NH during summer, especially  
672 over the south eastern US (Emmons et al., 2020, Fleming et al., 2015, Travis et al., 2016). While  
673 the horizontal resolution of 0.25 degrees is one of the highest for a global atmospheric chemistry  
674 forecast model, it is still not fine enough to resolve some of the meso-scale features of urban air  
675 pollution, which can lead to substantial model-observation mismatches when compared against  
676 urban air quality observations. Applying a bias-correction algorithm to the gridded model output,  
677 based on ML using historical observation-model comparisons, can lead to significant  
678 improvements of the model predictions over urban areas. This procedure, which can be  
679 automated as a post-processing step, offers an interesting option to provide highly localized  
680 forecasts at selected locations.

681

682 The GEOS-CF modeling system leverages components developed by the GEOS and the  
683 GEOS-Chem modeling communities and directly benefits from the continuous advancements  
684 provided by these groups. The current version of GEOS-CF (v1.0) incorporates GEOS-Chem  
685 v12.0.1. Several important updates have been added to GEOS-Chem since, and those will be  
686 included in future versions of GEOS-CF. This includes updates to the chemistry of isoprene  
687 (Bates and Jacob, 2019) and halogens (Wang et al., 2019), improved wet scavenging of aerosols  
688 (Luo et al., 2019; 2020), and updated ozone deposition over seawater (Pound et al., 2020). When  
689 implemented in future versions of GEOS-CF, these updates are expected to reduce the high bias  
690 observed in PM<sub>2.5</sub> and AOD as well as the high bias in surface ozone over the southern  
691 hemisphere.

692 Another model development focus will center around the assimilation of satellite observations of  
693 atmospheric constituents, which has been shown to lead to improved representation of  
694 atmospheric composition, in particular for longer-lived species such as O<sub>3</sub> and CO (Flemming et  
695 al., 2015). In its current form, GEOS-CF does not directly assimilate tropospheric trace gas  
696 observations, and the variability in constituent distribution is thus driven by the anthropogenic  
697 emission inventories, real-time biomass burning information, and the current meteorological  
698 state and its impact on dynamic emission sources such as biogenic emissions or sea salt aerosols.  
699 It should be noted that the anthropogenic emission inventories do not incorporate short-term,  
700 real-time changes in emissions, e.g., due to reduced human activities in the wake of the COVID-  
701 19 pandemic, and GEOS-CF v1.0 thus represents a business-as-usual estimate of the atmosphere  
702 (Keller et al., 2020). The inclusion of near real-time information for dynamic emission  
703 adjustment, e.g., based on traffic data or satellite observations, will be another model  
704 development focus.

705 GEOS-CF offers a new tool for academic researchers, air quality managers, and the  
706 public. Applications include flight campaign planning, support of satellite and other remote-  
707 sensing observations, interpretation of field campaign data (Dacic et al., 2020), and air quality  
708 research (Keller et al., 2020).

709

### 710 **Acknowledgements**

711 Resources supporting the model simulations were provided by the NASA Center for Climate  
712 Simulation at the Goddard Space Flight Center (<https://www.nccs.nasa.gov/services/discover>).  
713 CAK, KEK, DJJ, EWL, and SP acknowledge support by the NASA Modeling, Analysis and  
714 Prediction (MAP) Program.

715

### 716 **Data Availability Statement**

717 All model output is centrally stored at the NASA Center for Climate Simulation (NCCS). Public  
718 access to these archives is provided by the GMAO at  
719 [https://gmao.gsfc.nasa.gov/weather\\_prediction/GEOS-CF/data\\_access/](https://gmao.gsfc.nasa.gov/weather_prediction/GEOS-CF/data_access/) in the form of weather  
720 maps and through model output access tools, including OPeNDAP and Hypertext Transfer  
721 Protocol (HTTP).

### 722 **References**

723 Amos, H. M., D. J. Jacob, C. D. Holmes, J. A. Fisher, Q. Wang, R. M. Yantosca, E. S. Corbitt, E.  
724 Galarneau, A. P. Rutter, M. S. Gustin, A. Steffen, J. J. Schauer, J. A. Graydon, V. L. St. Louis,  
725 R. W. Talbot, E. S. Edgerton, Y. Zhang, and E. M. Sunderland (2012), Gas-Particle Partitioning  
726 of Atmospheric Hg(II) and Its Effect on Global Mercury Deposition, *Atmos. Chem.*  
727 *Phys.*, 12, 591-603.

728 Bacmeister, J. T., Suarez, M. J., & Robertson, F. R. (2006). Rain reevaporation, boundary layer  
729 convection interactions, and Pacific rainfall patterns in a AGCM. *Journal of the Atmospheric*  
730 *Sciences*, 63, 3383–3403. <https://doi.org/10.1175/JAS3791.1>

731 Bates, K.H., and D.J. Jacob (2019), A new model mechanism for atmospheric oxidation of  
732 isoprene: global effects on oxidants, nitrogen oxides, organic products, and secondary organic  
733 aerosol, *Atmos. Chem. Phys.*, 19, 9613-9640.

734 Bey, I., Jacob, D.J., Yantosca, R.M., Logan, J.A., Field, B.D., Fiore, A.M., Li, Q., Liu, H.Y.,  
735 Mickley, L.J., Schultz, M.G. (2001), Global modeling of tropospheric chemistry with assimilated

- 736 meteorology: Model description and evaluation. *J. Geophys. Res. Atmospheres* 106, 23073–  
737 23095. <https://doi.org/10.1029/2001JD000807>
- 738 Bhattacharjee, P. S., Wang, J., Lu, C.-H., and Tallapragada, V. (2018), The implementation of  
739 NEMS GFS Aerosol Component (NGAC) Version 2.0 for global multispecies forecasting at  
740 NOAA/NCEP – Part 2: Evaluation of aerosol optical thickness, *Geosci. Model Dev.*, 11, 2333–  
741 2351, <https://doi.org/10.5194/gmd-11-2333-2018>.
- 742 Bian, H., Prather, M.J. (2002), Fast-J2: Accurate Simulation of Stratospheric Photolysis in  
743 Global Chemical Models. *J. Atmospheric Chem.* 41, 281–296.  
744 <https://doi.org/10.1023/A:1014980619462>
- 745 Borovikov, A., Cullather, R., Kovach, R. et al. (2019), GEOS-5 seasonal forecast system. *Clim*  
746 *Dyn* 53, 7335–7361. <https://doi.org/10.1007/s00382-017-3835-2>
- 747 Buchard, V., Randles, C.A., Silva, A.M. da, Darmenov, A., Colarco, P.R., Govindaraju, R.,  
748 Ferrare, R., Hair, J., Beyersdorf, A.J., Ziemba, L.D., Yu, H., (2017), The MERRA-2 Aerosol  
749 Reanalysis, 1980 Onward. Part II: Evaluation and Case Studies. *J. Clim.* 30, 6851–6872.
- 750 Carn, S., (2019), Multi-Satellite Volcanic Sulfur Dioxide L4 Long-Term Global Database V3.  
751 <https://doi.org/10.5067/measures/so2/data404>
- 752 Carter, T. S., Heald, C. L., Jimenez, J. L., Campuzano-Jost, P., Kondo, Y., Moteki, N., Schwarz,  
753 J. P., Wiedinmyer, C., Darmenov, A. S., da Silva, A. M., and Kaiser, J. W. (2020), How  
754 emissions uncertainty influences the distribution and radiative impacts of smoke from fires in  
755 North America, *Atmos. Chem. Phys.*, 20, 2073–2097, <https://doi.org/10.5194/acp-20-2073-2020>.
- 756 Chen, T. and C. Guestrin (2016), XGBoost: A Scalable Tree Boosting System, *CoRR*,  
757 [abs/1603.02754](https://doi.org/10.1145/2939672.2939785), 785–794, <https://doi.org/10.1145/2939672.2939785>.
- 758 Chou, M.-D. (1990). Parameterizations for the absorption of solar radiation by O<sub>2</sub> and CO<sub>2</sub> with  
759 applications to climate studies. *Journal of Climate*, 3, 209–217.
- 760 Chou, M.-D. (1992). A solar radiation model for use in climate studies. *Journal of the*  
761 *Atmospheric Sciences*, 49, 762–772.
- 762 Chou, M.-D., & Suarez, M. J. (1994). An efficient thermal infrared radiation parameterization  
763 for use in general circulation models. *NASA Tech.Memorandum*, NASA/TM-1994–104606, Vol.  
764 3, 85 p.. Greenbelt, MD: NASA Goddard Space Flight Center.
- 765 Colarco, P., da Silva, A., Chin, M., Diehl, T. (2010). Online simulations of global aerosol  
766 distributions in the NASA GEOS-4 model and comparisons to satellite and ground-based aerosol  
767 optical depth. *J. Geophys. Res. Atmospheres* 115, D14207,  
768 <https://doi.org/10.1029/2009JD012820>.
- 769 Croft, B., Wentworth, G., Martin, R. et al. (2016), Contribution of Arctic seabird-colony  
770 ammonia to atmospheric particles and cloud-albedo radiative effect. *Nat Commun* 7, 13444.  
771 <https://doi.org/10.1038/ncomms13444>
- 772 Dacic, N., John T. Sullivan, K. Emma Knowland, Glenn M. Wolfe, Luke D. Oman, Timothy A.  
773 Berkoff, Guillaume P. Gronoff (2020), Evaluation of NASA's high-resolution global  
774 composition simulations: Understanding a pollution event in the Chesapeake Bay during the  
775 summer 2017 OWLETS campaign, *Atmospheric Environment*, Volume 222, 117133, ISSN  
776 1352-2310, <https://doi.org/10.1016/j.atmosenv.2019.117133>.

- 777 Darmenov, A.S., da Silva, A. (2015). The Quick Fire Emissions Dataset (QFED)—  
778 Documentation of versions 2.1, 2.2 and 2.4. *Technical Report Series on Global Modeling and*  
779 *Data Assimilation*. NASA//TM-2015-104606, Vol. 38, 212 pp.
- 780 Deeter, M. N., Edwards, D. P., Francis, G. L., Gille, J. C., Mao, D., Martinez-Alonso, S.,  
781 Worden, H. M., Ziskin, D., and Andreae, M. O. (2019), Radiance-based retrieval bias mitigation  
782 for the MOPITT instrument: the version 8 product, *Atmospheric Measurement Techniques*, 12,  
783 4561-4580, 10.5194/amt-12-4561-2019.
- 784 Delle Monache, L., T. Nipen, X. Deng, Y. Zhou, and R. Stull (2006), Ozone ensemble forecasts:  
785 2. A Kalman filter predictor bias correction, *J. Geophys. Res.*, 111, p. D05308,  
786 10.1029/2005JD006311
- 787 Delle Monache, L., Wilczak, J., Mckeen, S., Grell, G., Pagowski, M., Peckham, S., Stull, R.,  
788 Mchenry, J. & Mcqueen, J. (2008) A Kalman-filter bias correction method applied to  
789 deterministic, ensemble averaged and probabilistic forecasts of surface ozone, *Tellus B:*  
790 *Chemical and Physical Meteorology*, 60:2, 238-249, DOI: 10.1111/j.1600-0889.2007.00332.x
- 791 Djalalova, I., Delle Monache, L., and Wilczak J. (2015), PM2.5 analog forecast and Kalman  
792 filter post-processing for the Community Multiscale Air Quality (CMAQ) model, *Atmospheric*  
793 *Environment*, Volume 108, Pages 76-87, ISSN 1352-2310,  
794 <https://doi.org/10.1016/j.atmosenv.2015.02.021>.
- 795 Dlugokencky, E. J., L. P. Steele, P. M. Lang, and K. A. Masarie (1994), The growth rate and  
796 distribution of atmospheric methane, *J. Geophys. Res.*, 99, 17,021– 17,043,  
797 doi:10.1029/94JD01245.
- 798 Douglass, A. R., Stolarski, R. S., Strahan, S. E., & Connell, P. S. (2004). Radicals and reservoirs  
799 in the GMI chemistry and transport model: Comparison to measurements. *Journal of*  
800 *Geophysical Research*, 109, D16302. <https://doi.org/10.1029/2004JD004632>
- 801 Douglass, A. R., Strahan, S. E., Oman, L. D., & Stolarski, R. S. (2014). Understanding  
802 differences in chemistry climate model projections of stratospheric ozone. *Journal of*  
803 *Geophysical Research: Atmospheres*, 119, 4922–4939. <https://doi.org/10.1002/2013JD021159>
- 804 Duncan, B. N., Logan, J. A., Bey, I., Megretskaia, I. A., Yantosca, R. M., Novelli, P. C.,  
805 Rinsland, C. P. (2007). The global budget of CO, 1988– 1997: Source estimates and validation  
806 with a global model. *Journal of Geophysical Research*, 112, D22301. [https://doi.org/10.1029/](https://doi.org/10.1029/2007JD008459)  
807 [2007JD008459](https://doi.org/10.1029/2007JD008459)
- 808 Duncan, B. N. , L. N. Lamsal, A. M. Thompson, Y. Yoshida, Z. Lu, D. G. Streets, M. M.  
809 Hurwitz, and K. E. Pickering (2016), A space-based, high-resolution view of notable changes in  
810 urban NOx pollution around the world (2005–2014). *J. Geophys. Res.* 121, 976–996.
- 811 Eastham, S.D., Weisenstein, D.K., Barrett, S.R.H., (2014), Development and evaluation of the  
812 unified tropospheric–stratospheric chemistry extension (UCX) for the global chemistry- 34  
813 transport model GEOS-Chem. *Atmos. Environ.* 89, 52–63.
- 814 Emmons, L. K., Schwantes, R. H., Orlando, J. J., Tyndall, G., Kinnison, D., Lamarque, J.-F., et  
815 al. (2020). The Chemistry Mechanism in the Community Earth System Model version 2  
816 (CESM2). *Journal of Advances in Modeling Earth Systems*, 12, e2019MS001882.  
817 <https://doi.org/10.1029/2019MS001882>

- 818 Evans, M. J., and Jacob, D. (2005). Impact of new laboratory studies of N<sub>2</sub>O<sub>5</sub> hydrolysis on  
819 global model budgets of tropospheric nitrogen oxides, ozone, and OH, *Geophys. Res. Lett.*, 32,  
820 <http://doi.org/10.1029/2005gl022469>
- 821 Eyring, V., T. G. Shepherd, & D. W. Waugh (Eds.) (2010). SPARC report on the evaluation of  
822 chemistry-climate models (SPARC Rep. 5, WCRP-132, WMO/TD 1526). Retrieved from  
823 [http://www.atmosph.physics.utoronto.ca/SPARC/ccmval\\_final](http://www.atmosph.physics.utoronto.ca/SPARC/ccmval_final)
- 824 Frith, S. M., N. A. Kramarova, R. S. Stolarski, R. D. McPeters, P. K. Bhartia, and G. J. Labow  
825 (2014), Recent changes in total column ozone based on the SBUV Version 8.6 Merged Ozone  
826 Data Set, *J. Geophys. Res. Atmos.*, 119, 9735–9751, doi:10.1002/2014JD021889.
- 827 Flemming, J., Huijnen, V., Arteta, J., Bechtold, P., Beljaars, A., Blechschmidt, A.-M.,  
828 Diamantakis, M., Engelen, R. J., Gaudel, A., Inness, A., Jones, L., Josse, B., Katragkou, E.,  
829 Marecal, V., Peuch, V.-H., Richter, A., Schultz, M. G., Stein, O., and Tsikerdekis, A. (2015).  
830 Tropospheric chemistry in the Integrated Forecasting System of ECMWF, *Geosci. Model Dev.*,  
831 8, 975–1003, <https://doi.org/10.5194/gmd-8-975-2015>.
- 832 Fountoukis, C., Nenes, A. (2007). ISORROPIA II: a computationally efficient thermodynamic  
833 equilibrium model for K<sup>+</sup>–Ca<sup>2+</sup>–Mg<sup>2+</sup>–NH<sub>4</sub><sup>+</sup>–Na<sup>+</sup>–SO<sub>4</sub><sup>2-</sup>–NO<sub>3</sub><sup>-</sup>–Cl<sup>-</sup>–H<sub>2</sub>O aerosols.  
834 *Atmospheric Chem. Phys.* 7, 4639–4659
- 835 Garcia, R. R., & Boville, B. A. (1994). Downward control of the mean meridional circulation  
836 and temperature distribution of the polar winter stratosphere. *Journal of the Atmospheric*  
837 *Sciences*, 51, 2238–2245.
- 838 Gaubert, B., et al. (2016), Toward a chemical reanalysis in a coupled chemistry-climate model:  
839 An evaluation of MOPITT CO assimilation and its impact on tropospheric composition, *J.*  
840 *Geophys. Res. Atmos.*, 121, 7310–7343, doi:10.1002/2016JD024863.
- 841 Gelaro, R., McCarty, W., Suárez, M. J., Todling, R., Molod, A., Takacs, L., Randles, C. A.,  
842 Darmenov, A., Bosilovich, M. G., Reichle, R., Wargan, K., Coy, L., Cullather, R., Draper, C.,  
843 Akella, S., Buchard, V., Conaty, A., da Silva, A. M., Gu, W., Kim, G.-K., Koster, R., Lucchesi,  
844 R., Merkova, D., Nielsen, J. E., Partyka, G., Pawson, S., Putman, W., Rienecker, M., Schubert,  
845 S. D., Sienkiewicz, M., and Zhao, B. (2017). The Modern-Era Retrospective Analysis for  
846 Research and Applications, Version 2 (MERRA-2), *J. Climate*, 30, 5419–5454,  
847 <https://doi.org/10.1175/JCLI-D-16-0758.1>.
- 848 Giles, D. M., Sinyuk, A., Sorokin, M. G., Schafer, J. S., Smirnov, A., Slutsker, I., et al. (2019).  
849 Advancements in the Aerosol Robotic Network (AERONET) Version 3 database—Automated  
850 near-real-time quality control algorithm with improved cloud screening for Sun photometer  
851 aerosol optical depth (AOD) measurements. *Atmospheric Measurement Techniques*, 12, 169–  
852 209. <https://doi.org/10.5194/amt-12-169-2019>
- 853 Grange, S. K., Carslaw, D. C., Lewis, A. C., Boleti, E., and C. Hueglin (2018). Random forest  
854 meteorological normalisation models for Swiss PM 10 trend analysis, *Atmospheric Chemistry*  
855 *and Physics*, 18, 6223–6239, <https://doi.org/10.5194/acp-18-6223-430>.
- 856 Grange, S. K. and D. C. Carslaw (2019). Using meteorological normalisation to detect  
857 interventions in air quality time series, *Science of The Total Environment*, 653, 578–588,  
858 <https://doi.org/10.1016/j.scitotenv.2018.10.344>

- 859 Grosjean, D., and J. Harrison (1985), Response of chemiluminescence NO<sub>x</sub> analyzers and  
860 ultraviolet ozone analyzers to organic air pollutants, *Environ. Sci. Technol.*, 19, 862–865.
- 861 Hamill, T.M., J.S. Whitaker (2006), Probabilistic quantitative precipitation forecasts based on  
862 reforecast analogs: theory and application, *Mon. Weather Rev.*, 134, pp. 3209–3229,  
863 10.1175/MWR3237.1
- 864 Helfand, H. M., & Schubert, S. D. (1995). Climatology of the simulated Great Plains low-level  
865 jet and its contribution to the continental moisture budget of the United States. *Journal of*  
866 *Climate*, 8, 784–806.
- 867 Hill, C., DeLuca, C., Balaji, V., Suarez, M., & da Silva, A. (2004). Architecture of the earth  
868 system modeling framework. *Computing in Science and Engineering*, 6(1), 18–28.  
869 <https://doi.org/10.1109/MCISE.2004.1255817>
- 870 Honoré, C., et al. (2008), Predictability of European air quality: Assessment of 3 years of  
871 operational forecasts and analyses by the PREV'AIR system, *J. Geophys. Res.*, 113, D04301,  
872 doi:10.1029/2007JD008761.
- 873 Hu, L., Jacob, D. J., Liu, X., Zhang, Y., Zhang, L., Kim, P. S., Sulprizio, M. P., and Yantosca, R.  
874 M. (2017). Global budget of tropospheric ozone: Evaluating recent model advances with satellite  
875 (OMI), aircraft (IAGOS), and ozonesonde observations, *Atmos. Environ.*, 167, 323–334,  
876 <https://doi.org/10.1016/j.atmosenv.2017.08.036>.
- 877 Hu, L., Keller, C. A., Long, M. S., Sherwen, T., Auer, B., Da Silva, A., Nielsen, J. E., Pawson,  
878 S., Thompson, M. A., Trayanov, A. L., Travis, K. R., Grange, S. K., Evans, M. J., and Jacob, D.  
879 J. (2018). Global simulation of tropospheric chemistry at 12.5 km resolution: performance and  
880 evaluation of the GEOS-Chem chemical module (v10-1) within the NASA GEOS Earth system  
881 model (GEOS-5 ESM), *Geosci. Model Dev.*, 11, 4603–4620, [https://doi.org/10.5194/gmd-11-](https://doi.org/10.5194/gmd-11-4603-2018)  
882 4603-2018.
- 883 Ivatt, P. D. and Evans, M. J. (2020). Improving the prediction of an atmospheric chemistry  
884 transport model using gradient-boosted regression trees, *Atmos. Chem. Phys.*, 20, 8063–8082,  
885 <https://doi.org/10.5194/acp-20-8063-2020>.
- 886 Jacob, D. J., J. A. Logan, G. M. Gardner, R. M. Yevich, C. M. Spivakovsky, S. C. Wofsy, S.  
887 Sillman, and M. J. Prather (1993), Factors regulating ozone over the United States and its export  
888 to the global atmosphere, *J. Geophys. Res.*, 98, 14,817–14,826, doi:10.1029/98JD01224.
- 889 Jaeglé, L., Quinn, P.K., Bates, T.S., Alexander, B., Lin, J.-T. (2011). Global distribution of sea  
890 salt aerosols: new constraints from in situ and remote sensing observations. *Atmospheric Chem.*  
891 *Phys.* 11, 3137–3157.
- 892 Jaeglé, L., Shah, V., Thornton, J. A., Lopez-Hilfiker, F. D., Lee, B. H., McDuffie, E. E., Fibiger,  
893 D., Brown, S. S., Veres, P., Sparks, T. L., Ebben, C. J., Wooldridge, P. J., Kenagy, H. S., Cohen,  
894 R. C., Weinheimer, A. J., Campos, T. L., Montzka, D. D., Digangi, J. P., Wolfe, G. M., Hanisco,  
895 T., Schroder, J. C., Campuzano-Jost, P., Day, D. A., Jimenez, J. L., Sullivan, A. P., Guo, H., and  
896 Weber, R. J. (2018). Nitrogen Oxides Emissions, Chemistry, Deposition, and Export Over the  
897 Northeast United States During the WINTER Aircraft Campaign, *J. Geophys. Res.-Atmos.*, 123,  
898 12368–12393, <https://doi.org/10.1029/2018JD029133>.
- 899 Janssens-Maenhout, G., Crippa, M., Guizzardi, D., Dentener, F., Muntean, M., Pouliot, G.,  
900 Keating, T., Zhang, Q., Kurokawa, J., Wankmüller, R., Denier van der Gon, H., Kuenen, J. J. P.,

- 901 Klimont, Z., Frost, G., Darras, S., Koffi, B., and Li, M. (2015). HTAP\_v2.2: a mosaic of regional  
902 and global emission grid maps for 2008 and 2010 to study hemispheric transport of air pollution,  
903 *Atmos. Chem. Phys.*, 15, 11411–11432, <https://doi.org/10.5194/acp-15-11411-2015>.
- 904 Kang, D., R. Mathur, S.T. Rao, S. Yu (2008), Bias adjustment techniques for improving ozone  
905 air quality forecasts, *J. Geophys. Res.*, 113, p. D23308, 10.1029/2008JD010151
- 906 Keller, C.A., Long, M.S., Yantosca, R.M., Da Silva, A.M., Pawson, S., Jacob, D.J. (2014).  
907 HEMCO v1.0: a versatile, ESMF-compliant component for calculating emissions in atmospheric  
908 models. *Geosci. Model Dev.* 7, 1409–1417.
- 909 Keller, C. A., Evans, M. J., Knowland, K. E., Hasenkopf, C. A., Modekurty, S., Lucchesi, R. A.,  
910 Oda, T., Franca, B. B., Mandarino, F. C., Díaz Suárez, M. V., Ryan, R. G., Fakes, L. H., and  
911 Pawson, S. (2020), Global Impact of COVID-19 Restrictions on the Surface Concentrations of  
912 Nitrogen Dioxide and Ozone, *Atmos. Chem. Phys. Discuss.*, [https://doi.org/10.5194/acp-2020-](https://doi.org/10.5194/acp-2020-685)  
913 685, in review.
- 914 Kleist D. T., D. F. Parrish, J. C. Derber, R. Treadon, W.-S. Wu, and S. Lord, (2009). Introduction  
915 of the GSI into the NCEPs Global Data Assimilation System. *Wea. Forecasting*, 24, 1691- 1705.
- 916 Krol, M. and Lelieveld, J. (2003). Can the variability in tropospheric OH be deduced from  
917 measurements of 1,1,1-trichloroethane (methyl chloroform)?, *J. Geophys. Res.*, 108, 4125,  
918 [doi:10.1029/2002JD002423](https://doi.org/10.1029/2002JD002423).
- 919 Lamsal, L. N., Krotkov, N. A., Vasilkov, A., Marchenko, S., Qin, W., Yang, E.-S., Fasnacht, Z.,  
920 Joiner, J., Choi, S., Haffner, D., Swartz, W. H., Fisher, B., and Bucsele, E. (2020). OMI/Aura  
921 Nitrogen Dioxide Standard Product with Improved Surface and Cloud Treatments, *Atmos. Meas.*  
922 *Tech. Discuss.*, <https://doi.org/10.5194/amt-2020-200>, in review.
- 923 Lin, S. J. (2004). A vertically Lagrangian finite-volume dynamical core for global models. *Mon.*  
924 *Wea. Rev.*, 132, 2293–2307.
- 925 Liu, H., Jacob, D. J., Bey, I., and Yantosca, R. M. (2001). Constraints from <sup>210</sup>Pb and <sup>7</sup>Be on  
926 wet deposition and transport in a global three-dimensional chemical tracer model driven by  
927 assimilated meteorological fields, *J. Geophys. Res.*, 106, 12109- 12128,  
928 <http://doi.org/10.1029/2000jd900839>.
- 929 Liu, F., Choi, S., Li, C., Fioletov, V.E., McLinden, C.A., Joiner, J., Krotkov, N.A., Bian, H.,  
930 Janssens-Maenhout, G., Darmenov, A.S., da Silva, A.M. (2018). A new global anthropogenic  
931 SO<sub>2</sub> emission inventory for the last decade: a mosaic of satellite-derived and bottom-up  
932 emissions. *Atmospheric Chem. Phys.* 18, 16571–16586. [https://doi.org/10.5194/acp-18-16571-](https://doi.org/10.5194/acp-18-16571-2018)  
933 2018
- 934 Lock, A. P., Brown, A. R., Bush, M. R., Martin, G. M., & Smith, R. N. B. (2000). A new  
935 boundary layer mixing scheme. Part I: Scheme description and single-column model tests.  
936 *Monthly Weather Review*, 138, 3187–3199.
- 937 Long, M. S., Yantosca, R., Nielsen, J. E., Keller, C. A., da Silva, A., Sulprizio, M. P., Pawson,  
938 S., and Jacob, D. J. (2015). Development of a grid-independent GEOS-Chem chemical transport  
939 model (v9-02) as an atmospheric chemistry module for Earth system models, *Geoscientific*  
940 *Model Development*, 8, 595-602, <http://doi.org/10.5194/gmd-8-595-2015>

- 941 Louis, J., & Geleyn, J. (1982). A short history of the PBL parameterization at ECMWF. In  
942 Proceedings of the ECMWF workshop on planetary boundary layer parameterization (pp. 59–  
943 80). Reading, UK: ECMWF.
- 944 Lucchesi, R. (2015). File Specification for GEOS-5 FP-IT. GMAO Office Note No. 2 (Version  
945 1.4) 58 pp, available from [http://gmao.gsfc.nasa.gov/pubs/office\\_notes.php](http://gmao.gsfc.nasa.gov/pubs/office_notes.php).
- 946 Luo, G., Yu, F., and Schwab, J. (2019). Revised treatment of wet scavenging processes  
947 dramatically improves GEOS-Chem 12.0.0 simulations of surface nitric acid, nitrate, and  
948 ammonium over the United States, *Geosci. Model Dev.*, 12, 3439–3447,  
949 <https://doi.org/10.5194/gmd-12-3439-2019>.
- 950 Luo, G., F. Yu, and J. Moch (2020). Further improvement of wet process treatments in GEOS-  
951 Chem v12.6.0: impact on global distributions of aerosols and aerosol precursors, *Geosci. Model*  
952 *Dev.*, 13, 2879-2903.
- 953 Mao, J., Jacob, D.J., Evans, M.J., Olson, J.R., Ren, X., Brune, W.H., Clair, J.M.St., Crouse,  
954 J.D., Spencer, K.M., Beaver, M.R., Wennberg, P.O., Cubison, M.J., Jimenez, J.L., Fried, A.,  
955 Weibring, P., Walega, J.G., Hall, S.R., Weinheimer, A.J., Cohen, R.C., Chen, G., Crawford, J.H.,  
956 McNaughton, C., Clarke, A.D., Jaeglé, L., Fisher, J.A., Yantosca, R.M., Le Sager, P., Carouge,  
957 C. (2010). Chemistry of hydrogen oxide radicals (HOx) in the Arctic troposphere in spring.  
958 *Atmospheric Chem. Phys.* 10, 5823–5838. <https://doi.org/10.5194/acp-10-5823-2010>
- 959 Mao, J., Paulot, F., Jacob, D.J., Cohen, R.C., Crouse, J.D., Wennberg, P.O., Keller, C.A.,  
960 Hudman, R.C., Barkley, M.P., Horowitz, L.W. (2013). Ozone and organic nitrates over the  
961 eastern United States: Sensitivity to isoprene chemistry. *J. Geophys. Res. Atmospheres* 118,  
962 11,256–11,268.
- 963 Marais, E. A., Jacob, D. J., Jimenez, J. L., Campuzano-Jost, P., Day, D. A., Hu, W., Krechmer,  
964 J., Zhu, L., Kim, P. S., Miller, C. C., Fisher, J. A., Travis, K., Yu, K., Hanisco, T. F., Wolfe, G.  
965 M., Arkinson, H. L., Pye, H. O. T., Froyd, K. D., Liao, J., and McNeill, V. F. (2016). Aqueous-  
966 phase mechanism for secondary organic aerosol formation from isoprene: application to the  
967 southeast United States and co-benefit of SO<sub>2</sub> emission controls, *Atmos. Chem. Phys.*, 16, 1603-  
968 1618, <http://doi.org/10.5194/acp-16-1603-2016>.
- 969 Marais, E. and C. Wiedinmyer (2016), Air quality impact of Diffuse and Inefficient Combustion  
970 Emissions in Africa (DICE-Africa), *Environ. Sci. Technol.*, 50(19), 10739–10745,  
971 [doi:10.1021/acs.est.6b02602](https://doi.org/10.1021/acs.est.6b02602).
- 972 Marécal, V., et al. (2015). A regional air quality forecasting system over Europe: the MACC-II  
973 daily ensemble production, *Geosci. Model Dev.*, 8, 2777–2813, <https://doi.org/10.5194/gmd-8-2777-2015>.
- 975 Martin, R. V., Jacob, D. J., Yantosca, R. M., Chin, M., and Ginoux, P. (2003). Global and  
976 regional decreases in tropospheric oxidants from photochemical effects of aerosols, *J. Geophys.*  
977 *Res.*, 108, n/a-n/a, <http://doi.org/10.1029/2002jd002622>.
- 978 McFarlane, N. A. (1987). The effect of orographically excited gravity-wave drag on the  
979 circulation of the lower stratosphere and troposphere. *Journal of the Atmospheric Sciences*, 44,  
980 1775–1800.
- 981 McKeen S., J. Wilczak, G. Grell, I. Djalalova, S. Peckham, E.-Y. Hsie, W. Gong, V. Bouchet, S.  
982 Menard, R. Moffet, J. McHenry, J. McQueen, Y. Tang, G.R. Carmichael, M. Pagowski, A. Chan,

- 983 T. Dye, G. Frost, P. Lee, R. Mathur (2005), Assessment of an ensemble of seven real-time ozone  
984 forecasts over eastern North America during the summer of 2004, *J. Geophys. Res.*, 110, p.  
985 D21307, 10.1029/2005JD005858
- 986 Miller, C., Jacob, D. J., Marais, E. A., Yu, K., Travis, K. R., Kim, P. S., Fisher, J. A., Zhu, L.,  
987 Wolfe, G. M., Hanisco, T. F., Keutsch, F. N., Kaiser, J., Min, K.-E., Brown, S. S., Washenfelder,  
988 R. A., González Abad, G., and Chance, K. (2017). Glyoxal yield from isoprene oxidation and  
989 relation to formaldehyde: chemical mechanism, constraints from SENEX aircraft observations,  
990 and interpretation of OMI satellite data, *Atmos. Chem. Phys.*, 17, 8725–8738,  
991 <https://doi.org/10.5194/acp-17-8725-2017>.
- 992 Molod, A., Takacs, L. L., Suarez, M. J., Bacmeister, J. T., Song, I.-S., and Eichmann, A. (2012).  
993 The GEOS-5 Atmospheric General Circulation Model: Mean Climate and Development from  
994 MERRA to Fortuna. NASA Tech. Memo. 104606, Vol. 28, Tech. Rep. Series on Global  
995 Modeling and Data Assimilation, edited by: Suarez, M. J., 117 pp.
- 996 Molod, A., Partyka, G., & Suarez, M. (2013). The impact of limiting ocean roughness on GEOS-  
997 5 AGCM tropical cyclone forecasts. *Geophysical Research Letters*, 40, 411–416.  
998 <https://doi.org/10.1029/2012GL053979>
- 999 Molod, A., Takacs, L., Suarez, M., and Bacmeister, J. (2015). Development of the GEOS-5  
1000 atmospheric general circulation model: evolution from MERRA to MERRA2, *Geosci. Model*  
1001 *Dev.*, 8, 1339–1356, doi:10.5194/gmd-8-1339-2015.
- 1002 Molod, A., E. Hackert, Y. Vikhliav, B. Zhao, D. Barahona, G. Vernieres, A. Borovikov, R. M.  
1003 Kovach, J. Marshak, S. Schubert, Z. Li, Y.-K. Lim, L. C. Andrews, R. Cullather, R. Koster, D.  
1004 Achuthavarier, J. Carton, L. Coy, J. L. M. Freire, K. M. Longo, K. Nakada, and S. Pawson,  
1005 (2020). GEOS-S2S Version 2: The GMAO High Resolution Coupled Model and Assimilation  
1006 System for Seasonal Prediction. *J. Geophys. Res. - Atmos.*, 125, e2019JD031767. doi:  
1007 10.1029/2019JD031767.
- 1008 Monks, S. A., Arnold, S. R., Emmons, L. K., Law, K. S., Turquety, S., Duncan, B. N.,  
1009 Flemming, J., Huijnen, V., Tilmes, S., Langner, J., Mao, J., Long, Y., Thomas, J. L., Steenrod, S.  
1010 D., Raut, J. C., Wilson, C., Chipperfield, M. P., Diskin, G. S., Weinheimer, A., Schlager, H., and  
1011 Ancellet, G. (2015). Multi-model study of chemical and physical controls on transport of  
1012 anthropogenic and biomass burning pollution to the Arctic, *Atmos. Chem. Phys.*, 15, 3575–3603,  
1013 doi:10.5194/acp-15-3575-2015.
- 1014 Montzka, S. A., Spivakovsky, C. M., Butler, J. H., Elkins, J. W., Lock, L. T., and Mondeel, D. J.  
1015 (2000). New observational constraints, for atmospheric hydroxyl on global and hemispheric  
1016 scales, *Science*, 288, 500–503.
- 1017 Moorthi, S., & Suarez, M. J. (1992). Relaxed Arakawa Schubert: A parameterization of moist  
1018 convection for general circulation models. *Monthly Weather Review*, 120, 978–1002.
- 1019 Murray, L. T., D. J. Jacob, J. A. Logan, R. C. Hudman, and W. J. Koshak (2012), Optimized  
1020 regional and interannual variability of lightning in a global chemical transport model constrained  
1021 by LIS/OTD satellite data, *J. Geophys. Res.*, 117, D20307, doi:10.1029/2012JD017934.
- 1022 Naik, V., Voulgarakis, A., Fiore, A. M., Horowitz, L. W., Lamarque, J.-F., Lin, M., Prather, M.  
1023 J., Young, P. J., Bergmann, D., Cameron-Smith, P. J., Cionni, I., Collins, W. J., Dalsøren, S. B.,  
1024 Doherty, R., Eyring, V., Faluvegi, G., Folberth, G. A., Josse, B., Lee, Y. H., MacKenzie, I. A.,

- 1025 Nagashima, T., van Noije, T. P. C., Plummer, D. A., Righi, M., Rumbold, S. T., Skeie, R.,  
1026 Shindell, D. T., Stevenson, D. S., Strode, S., Sudo, K., Szopa, S., and Zeng, G. (2013).  
1027 Preindustrial to present-day changes in tropospheric hydroxyl radical and methane lifetime from  
1028 the Atmospheric Chemistry and Climate Model Intercomparison Project (ACCMIP), *Atmos.*  
1029 *Chem. Phys.*, 13, 5277–5298, doi:10.5194/acp-13-5277-2013.
- 1030 Nielsen, J. E., S. Pawson, A. Molod, B. Auer, A. M. da Silva, A. R. Douglass, B. N. Duncan, Q.  
1031 Liang, M. E. Manyin, L. D. Oman, W. M. Putman, S. E. Strahan, and K. Wargan (2017).  
1032 Chemical Mechanisms and their Applications in the Goddard Earth Observing System (GEOS)  
1033 Earth System Model. *J. Adv. Model. Earth Syst.*, 9, 3019–3044. DOI: 10.1002/2017MS001011.
- 1034 Oda, T., Maksyutov, S., and Andres, R. J. (2018). The Open-source Data Inventory for  
1035 Anthropogenic CO<sub>2</sub>, version 2016 (ODIAC2016): a global monthly fossil fuel CO<sub>2</sub> gridded  
1036 emissions data product for tracer transport simulations and surface flux inversions, *Earth Syst.*  
1037 *Sci. Data*, 10, 87–107, <https://doi.org/10.5194/essd-10-87-2018>.
- 1038 Oman, L. D., & Douglass, A. R. (2014). Improvements in total column ozone in GEOSCCM and  
1039 comparisons with a new ozone-depleting substances scenario. *Journal of Geophysical Research:*  
1040 *Atmospheres*, 119, 5613–5624. <https://doi.org/10.1002/2014JD021590>
- 1041 Orbe, C., L. D. Oman, S. E. Strahan, D. W. Waugh, L. L. Takacs, S. Pawson, and A. M. Molod  
1042 (2017). Large-Scale Atmospheric Transport in GEOS Replay Simulations. *J. Adv. Model. Earth*  
1043 *Sy.*, 9, 7, 2545–2560. DOI: 10.1002/2017MS001053.
- 1044 Park, R. J., Jacob, D. J., Chin, M., and Martin, R. V. (2003). Source of carbonaceous aerosols  
1045 over the United States and implications for natural visibility, *J. Geophys. Res.*, 108, 4355,  
1046 <https://doi.org/10.1029/2002JD003190>.
- 1047 Park, R. J., Jacob, D. J., Field, B. D., Yantosca, R. M., and Chin, M. (2004). Natural and  
1048 transboundary pollution influences on sulfate-nitrate-ammonium aerosols in the United States:  
1049 Implications for policy, *J Geophys Res-Atmos*, 109, <http://doi.org/10.1029/2003jd004473>
- 1050 Parrella, J.P., Jacob, D.J., Liang, Q., Zhang, Y., Mickley, L.J., Miller, B., Evans, M.J., Yang, X.,  
1051 Pyle, J.A., Theys, N., Van Roozendaal, M. (2012). Tropospheric bromine chemistry:  
1052 implications for present and pre-industrial ozone and mercury. *Atmospheric Chem. Phys.* 12,  
1053 6723–6740. <https://doi.org/10.5194/acp-12-6723-2012>
- 1054 Patra, P., Krol, M., Montzka, S., Arnold, T., Atlas, E. L., Lintner, B., Stephens, B., Xiang, B.,  
1055 Elkins, J., Fraser, P., et al. (2014). Observational evidence for interhemispheric hydroxyl-radical  
1056 parity, *Nature*, 513, 219.
- 1057 Pawson, S., Stajner, I., Kawa, S. R., Hayashi, H., Tan, W., Nielsen, J. E., . . . Livesey, N. J.  
1058 (2007). Stratospheric transport using six-hour averaged winds from a data assimilation system.  
1059 *Journal of Geophysical Research*, 112, D23103. <https://doi.org/10.1029/2006JD007673>
- 1060 Petetin, H., Bowdalo, D., Soret, A., Guevara, M., Jorba, O., Serradell, K., and Pérez García-  
1061 Pando, C. (2020). Meteorology-normalized impact of the COVID-19 lockdown upon  
1062 NO<sub>2</sub> pollution in Spain, *Atmos. Chem. Phys.*, 20, 11119–11141, [https://doi.org/10.5194/acp-20-](https://doi.org/10.5194/acp-20-11119-2020)  
1063 11119-2020.
- 1064 Pound, R. J., Sherwen, T., Helmig, D., Carpenter, L. J., and Evans, M. J. (2020). Influences of  
1065 oceanic ozone deposition on tropospheric photochemistry, *Atmos. Chem. Phys.*, 20, 4227–4239,  
1066 <https://doi.org/10.5194/acp-20-4227-2020>.

- 1067 Price, C., and D. Rind (1992), A simple lightning parameterization for calculating global  
1068 lightning distributions, *J. Geophys. Res.*, 97, 9919–9933, doi:10.1029/92JD00719.
- 1069 Price, C., and D. Rind (1993), What determines the cloud-to-ground lightning fraction in  
1070 thunderstorms, *Geophys. Res. Lett.*, 20(6), 463–466, doi:10.1029/93GL00226.
- 1071 Price, C., and D. Rind (1994), Modeling global lightning distributions in a general-circulation  
1072 model, *Mon. Weather Rev.*, 122(8), 1930–1939, doi:10.1175/1520-  
1073 0493(1994)122<1930:MGLDIA>2.0.CO;2
- 1074 Prinn, R. G., Huang, J., Weiss, R. F., Cunnold, D. M., Fraser, P. J., Simmonds, P. G.,  
1075 McCulloch, A., Harth, C., Salameh, P., O’Doherty, S., Wang, R. H. J., Porter, L., and Miller, B.  
1076 R. (2001). Evidence for substantial variations of atmospheric hydroxyl radicals over the past two  
1077 decades, *Science*, 292, 1882–1888.
- 1078 Putman, W. and Lin, S.-J. (2007). Finite Volume Transport on Various Cubed Sphere Grids. *J.*  
1079 *Comput. Phys.*, 227, 55–78. doi:10.1016/j.jcp.2007.07.022.
- 1080 Pye, H.O.T., Liao, H., Wu, S., Mickley, L.J., Jacob, D.J., Henze, D.K., Seinfeld, J.H. (2009). 36  
1081 Effect of changes in climate and emissions on future sulfate-nitrate-ammonium aerosol levels in  
1082 the United States. *J. Geophys. Res. Atmospheres* 114, D01205.  
1083 <https://doi.org/10.1029/2008JD010701>
- 1084 Randles, C. A., and Coauthors (2017). The MERRA-2 aerosol reanalysis, 1980 onward, Part I:  
1085 System description and data assimilation evaluation. *J. Climate*, 30, 6823–6850,  
1086 doi:<https://doi.org/10.1175/JCLI-D-16-0609.1>
- 1087 Ridley, D. A., Heald, C. L., and Ford, B. J. (2012). North African dust export and impacts: an  
1088 integrated satellite and model perspective, *J. Geophys. Res.*, 117, D02202,  
1089 <https://doi.org/10.1029/2011JD016794>.
- 1090 Rienecker, M.M., M.J. Suarez, R. Todling, J. Bacmeister, L. Takacs, H.-C. Liu, W. Gu, M.  
1091 Sienkiewicz, R.D. Koster, R. Gelaro, I. Stajner, and E. Nielsen (2008). The GEOS-5 Data  
1092 Assimilation System - Documentation of Versions 5.0.1, 5.1.0, and 5.2.0. Technical Report  
1093 Series on Global Modeling and Data Assimilation 104606, Vol. 27.
- 1094 Rienecker and Coauthors (2011). MERRA - NASA's Modern-Era Retrospective Analysis for  
1095 Research and Applications. *J. Climate*, 24, 3624–3648, doi:10.1175/JCLI-D-11-00015.1.
- 1096 Rotman, D.A., Tannahill, J.R., Kinnison, D.E., Connell, P.S., Bergmann, D., Proctor, D.,  
1097 Rodriguez, J.M., Lin, S.J., Rood, R.B., Prather, M.J., Rasch, P.J., Considine, D.B., Ramarosan,  
1098 R., Kawa, S.R. (2001). Global modeling initiative assessment model: model description,  
1099 integration, and testing of the transport shell. *Journal of Geophysical Research* 106, 1669e1691.
- 1100 Sandu, A., Sander, R. (2006). Technical note: Simulating chemical systems in Fortran90 and  
1101 Matlab with the Kinetic PreProcessor KPP-2.1. *Atmospheric Chem. Phys.* 6, 187–195.  
1102 <https://doi.org/10.5194/acp-6-187-2006>
- 1103 Sherwen, T., Schmidt, J.A., Evans, M.J., Carpenter, L.J., Gros smann, K., Eastham, S.D., Jacob,  
1104 D.J., Dix, B., Koenig, T.K., Sinreich, R., Ortega, I., Volkamer, R., Saiz-Lopez, A., Prados-  
1105 Roman, C., Mahajan, A.S., Ordóñez, C. (2016). Global impacts of tropospheric halogens (Cl, Br,  
1106 I) on oxidants and composition in GEOS-Chem. *Atmospheric Chem. Phys.* 16, 12239–12271.

- 1107 Schumann, U., and H. Huntrieser (2007), The global lightning-induced nitrogen oxides source,  
1108 *Atmos. Chem. Phys.*, 7(14), 3823–3907, doi:10.5194/acp-7-3823-2007.
- 1109 Seinfeld, J.H. and S.N. Pandis (2016). Atmospheric Chemistry and Physics: From Air Pollution  
1110 to Climate Change. John Wiley & Sons, Hoboken.
- 1111 Shah, V., Jacob, D. J., Li, K., Silvern, R. F., Zhai, S., Liu, M., Lin, J., and Zhang, Q. (2020).  
1112 Effect of changing NO<sub>x</sub> lifetime on the seasonality and long-term trends of satellite-observed  
1113 tropospheric NO<sub>2</sub> columns over China, *Atmos. Chem. Phys.*, 20, 1483–1495,  
1114 <https://doi.org/10.5194/acp-20-1483-2020>.
- 1115 Shindell, D. T., et al. (2006), Multimodel simulations of carbon monoxide: Comparison with  
1116 observations and projected near-future changes, *J. Geophys. Res.*, 111, D19306,  
1117 doi:10.1029/2006JD007100.
- 1118 Sillman, S., and P. J. Samson (1995), Impact of temperature on oxidant photochemistry in urban,  
1119 polluted rural and remote environments, *J. Geophys. Res.*, 100, 11,497–11,508,  
1120 doi:10.1029/94JD02146.
- 1121 Solomon, S., Portmann, R. W., Sasaki, T., Hofmann, D. J., and Thompson, D. W. J. (2005). Four  
1122 decades of ozonesonde measurements over Antarctica, *Journal of Geophysical Research-*  
1123 *Atmospheres*, 110, 10.1029/2005jd005917.
- 1124 Spivakovsky, C. M., Logan, J. A., Montzka, S. A., Balkanski, Y. J., Foreman-Fowler, M., Jones,  
1125 D. B. A., Horowitz, L. W., Fusco, A. C., Brenninkmeijer, C. A. M., Prather, M. J., Wofsy, S. C.,  
1126 and McElroy, M. B. (2000). Three-dimensional climatological distribution of tropospheric OH:  
1127 Update and evaluation, *J. Geophys. Res.*, 105, 8931–8980.
- 1128 Steinbacher, M., Zellweger, C., Schwarzenbach, B., Bugmann, S., Buchmann, B., Ordóñez, C.,  
1129 Prevot, A. S. H., and Hueglin, C. (2007), Nitrogen oxide measurements at rural sites in  
1130 Switzerland: Bias of conventional measurement techniques, *J. Geophys. Res.*, 112, D11307,  
1131 doi:10.1029/2006JD007971.
- 1132 Streets, D.G., Canty T., Carmichael, G.R. , de Foy, B. Dickerson, R.R, Duncan, B.N., Edwards,  
1133 D.P. , Haynes, J.A., Henze, D.K., Houyoux, M.R., Jacob, D.J., Krotkov, N.A., Lamsal, L.N., Liu,  
1134 Y., Lu, Z., Martin, R.V., Pfister, G.G., Pinder, R.W., Salawitch, R.J., and K.J. Wecht (2013),  
1135 Emissions estimation from satellite retrievals: A review of current capability, *Atmospheric*  
1136 *Environment*, Volume 77, Pages 1011-1042, <https://doi.org/10.1016/j.atmosenv.2013.05.051>.
- 1137 Strode, S. A., Duncan, B. N., Yegorova, E. A., Kouatchou, J., Ziemke, J. R., and Douglass, A. R.  
1138 (2015). Implications of carbon monoxide bias for methane lifetime and atmospheric composition  
1139 in chemistry climate models, *Atmos. Chem. Phys.*, 15, 11789–11805, [https://doi.org/10.5194/acp-](https://doi.org/10.5194/acp-15-11789-2015)  
1140 [15-11789-2015](https://doi.org/10.5194/acp-15-11789-2015).
- 1141 Stettler, M., Eastham, S., and Barrett, S. (2011). Air quality and public health impacts of UK  
1142 airports. Part I: Emissions, *Atmos. Environ.*, 45, 5415–5424,  
1143 doi:10.1016/j.atmosenv.2011.07.012, 2011.
- 1144 Strahan, S.E., B.N. Duncan and P. Hoor (2007). Observationally-derived diagnostics of transport  
1145 in the lowermost stratosphere and their application to the GMI chemistry transport model ,  
1146 *Atmos. Chem. Phys.*, 7, 2435-2445.

- 1147 Suarez, M., Trayanov, A., Hill, C., Schopf, P., & Vikhliayev, Y. (2007). MAPL: A high-level  
1148 programming paradigm to support more rapid and robust encoding of hierarchical trees of  
1149 interacting high-performance components. In Proceedings of the 2007 symposium on component  
1150 and framework technology in high-performance and scientific computing (pp. 11–20).  
1151 <https://doi.org/10.1145/1297385.1297388>
- 1152 Tarasova, O. A., and A. Y. Karpetchko (2003), Accounting for local meteorological effects in  
1153 the ozone time-series of Lovozero (Kola Peninsula), *Atmos. Chem. Phys.*, 3(4), 941–949,  
1154 doi:10.5194/acp-3-941-2003.
- 1155 Thompson, A. M., Witte, J. C., Sterling, C., Jordan, A., Johnson, B. J., Oltmans, S. J., Fujiwara,  
1156 M., Vomel, H., Allaart, M., Piters, A., Coetzee, G. J. R., Posny, F., Corrales, E., Diaz, J. A.,  
1157 Felix, C., Komala, N., Lai, N., Nguyen, H. T. A., Maata, M., Mani, F., Zainal, Z., Ogino, S. Y.,  
1158 Paredes, F., Penha, T. L. B., da Silva, F. R., Sallons-Mitro, S., Selkirk, H. B., Schmidlin, F. J.,  
1159 Stubi, R., and Thiongo, K. (2017). First Reprocessing of Southern Hemisphere Additional  
1160 Ozonesondes (SHADOZ) Ozone Profiles (1998-2016): 2. Comparisons With Satellites and  
1161 Ground-Based Instruments, *Journal of Geophysical Research-Atmospheres*, 122, 13000-13025,  
1162 10.1002/2017jd027406.
- 1163 Travis, K. R., Jacob, D. J., Fisher, J. A., Kim, P. S., Marais, E. A., Zhu, L., Yu, K., Miller, C. C.,  
1164 Yantosca, R. M., Sulprizio, M. P., Thompson, A. M., Wennberg, P. O., Crouse, J. D., St. Clair,  
1165 J. M., Cohen, R. C., Laughner, J. L., Dibb, J. E., Hall, S. R., Ullmann, K., Wolfe, G. M., Pollack,  
1166 I. B., Peischl, J., Neuman, J.A., and Zhou, X. (2016). Why do models overestimate surface ozone  
1167 in the Southeast United States?, *Atmos. Chem. Phys.*, 16, 13561–13577,  
1168 <https://doi.org/10.5194/acp-16-13561-2016>.
- 1169 Travis, K. R. and Jacob, D. J. (2019). Systematic bias in evaluating chemical transport models  
1170 with maximum daily 8 h average (MDA8) surface ozone for air quality applications: a case study  
1171 with GEOS-Chem v9.02, *Geosci. Model Dev.*, 12, 3641–3648, [https://doi.org/10.5194/gmd-12-](https://doi.org/10.5194/gmd-12-3641-2019)  
1172 3641-2019.
- 1173 Wang, Q., Jacob, D.J., Spackman, J.R., Perring, A.E., Schwarz, J.P., Moteki, N., Marais, E.A.,  
1174 Ge, C., Wang, J., Barrett, S.R.H. (2014). Global budget and radiative forcing of black carbon  
1175 aerosol: Constraints from pole-to-pole (HIPPO) observations across the Pacific. *J. Geophys. Res.*  
1176 *Atmospheres* 119, 195–206.
- 1177 Wang, X., D.J. Jacob, M.P. Sulprizio, S.D. Eastham, L. Zhu, Q. Chen, B. Alexander, T.  
1178 Sherwen, M.J. Evans, B.H. Lee, J.D. Haskins, F.D. Lopez-Hilfike, J.A. Thornton, G.L. Huey,  
1179 and H. Liao (2019), The role of chlorine in global tropospheric chemistry, *Atmos. Chem. Phys.*,  
1180 19, 3981-4003.
- 1181 Wargan, K., S. Pawson, M. A. Olsen, J. C. Witte, A. R. Douglass, J. R. Ziemke, S. E. Strahan,  
1182 and J. E. Nielsen (2015). The Global Structure of Upper Troposphere-Lower Stratosphere Ozone  
1183 in GEOS-5: A Multi-Year Assimilation of EOS Aura Data. *J. Geophys. Res. - Atmos.*, 120, 2013-  
1184 2036. doi: 10.1002/2014JD022493.
- 1185 Wargan, K., N. Kramarova, B. Weir, S. Pawson, and S. Davis (2020). Towards a reanalysis of  
1186 stratospheric ozone for trend studies: Assimilation of the Aura Microwave Limb Sounder and  
1187 Ozone Mapping and Profiler Suite Limb Profiler data. *J. Geophys. Res. - Atmos.*, 125,  
1188 e2019JD031892. doi: 10.1029/2019JD031892.

- 1189 Waugh, D. W., & Eyring, V. (2008). Quantitative performance metrics for stratospheric-  
1190 resolving chemistry-climate models. *Atmospheric Chemistry and Physics*, 8, 5699–5713.  
1191 <https://doi.org/10.5194/acp-8-5699-2008>
- 1192 Wesely, M. L. (1989). Parameterization of Surface Resistances to Gaseous Dry Deposition in  
1193 Regional-Scale Numerical-Models, *Atmos. Environ.*, 23, 1293-1304, <http://doi.org/Doi>  
1194 [10.1016/0004-6981\(89\)90153-4](https://doi.org/10.1016/0004-6981(89)90153-4).
- 1195 Wilczak, J., S.A. McKeen, I. Djalalova, et al. (2006). Bias-corrected ensemble and probabilistic  
1196 forecasts of surface ozone over eastern North America during the summer of 2004, *J. Geophys.*  
1197 *Res.*, 111 (D23S28), [10.1029/2006JD007598](https://doi.org/10.1029/2006JD007598)
- 1198 Winer, A. M., J. W. Peters, J. P. Smith, and J. N. Pitts Jr. (1974), Response of commercial  
1199 chemiluminescence NO–NO<sub>2</sub> analyzers to other nitrogen-containing compounds, *Environ. Sci.*  
1200 *Technol.*, 8, 1118–1121.
- 1201 Wu, W.-S., R.J. Purser and D.F. Parrish (2002). Three-dimensional variational analysis with  
1202 spatially inhomogeneous covariances. *Mon. Wea. Rev.*, 130, 2905-2916.
- 1203 Zhang, Y., Jacob, D. J., Lu, X., Maasackers, J. D., Scarpelli, T. R., Sheng, J.-X., Shen, L., Qu,  
1204 Z., Sulprizio, M. P., Chang, J., Bloom, A. A., Ma, S., Worden, J., Parker, R. J., and Boesch, H.  
1205 (2020), Attribution of the accelerating increase in atmospheric methane during 2010–2018 by  
1206 inverse analysis of GOSAT observations, *Atmos. Chem. Phys. Discuss.*,  
1207 <https://doi.org/10.5194/acp-2020-964>, in review.